Chapter 3

A linear operator relating interval velocities and migration velocities

3.1 INTRODUCTION

In the preceding chapter I described how to find prestack time-migration velocities, and showed that, for complex structure, they provide a natural generalization of stacking velocities. Migration velocities can be evaluated similarly to conventional stacking velocities, but are corrected for the structural effects that can drastically bias stacking velocities. However, these migration velocities will equal the medium acoustic velocity only when that velocity is constant. What do these "velocities" mean when the medium velocity is varying?

Although I use migration operators formulated in the frequency domain in the methods presented in chapter 2, they may be visualized also in the time-space domain. In that domain, migration is a weighted sum over a diffraction surface, and the time-migration velocities specify the curvature of this surface. Thus, these migration "velocities" are not physical velocities, but instead are simply free parameters in the prestack time-migration operator. What one really requires are the interval velocities, particularly when the velocities vary substantially laterally. For weak lateral velocity variation, a time-migrated image provides an adequate picture of the subsurface, but for stronger lateral variation, depth migration is needed, for which one must know the true interval velocities.

Clearly, however, the observed migration velocities are not simply arbitrary, but depend on the underlying interval velocities. In general, the relation between the two is complicated and non-linear, so in this chapter I derive a linear approximation describing the changes in migration velocities caused by small perturbations in interval velocities. As I show below, this operator may be viewed as a filtered version of more conventional tomographic back-projection. Like conventional tomography, this method uses kinematic, or traveltime, information, but rather than requiring direct

measurement of the traveltimes associated with specified reflection events, this approach uses the migration velocities, which are themselves functions of the traveltimes. The "filter" in this variant of tomography thus unscrambles the relation between the observed migration velocities and the traveltimes that implicitly underlie this computation. This chapter focuses on the derivation and properties of the linear operator and its relation to traveltime tomography; chapter 4 discusses the use of this operator to invert migration velocities for interval velocities. In both chapters, for simplicity, I restrict the discussion to two-dimensional data.

3.2 A LINEAR OPERATOR

It is conceptually and notationally easier to work here with slowness rather than velocity, because traveltimes are the integrals of slowness, rather than of velocity. Write the migration slowness $\mathbf{s}$ as a function of midpoint y and zero-offset time τ, and the interval slowness $\mathbf{m}$ as a function of lateral position x and depth z. The relation between these two slownesses will generally be nonlinear. Inverting migration slownesses for interval slownesses thus requires an iterative solution, using a linear approximation to find a gradient direction to update a model at each step. What is needed is an expression for $\partial s_d / \partial m_a$, relating a change in interval slowness at a particular model anomaly point $\mathbf{a}=(x_a, z_a)$ to the resulting change in observed migration slowness at some point $\mathbf{d}=(x_d, z_d)$ in the data space. That is, one wants a linear operator $\mathbf{G}$ such that

$$\Delta \mathbf{s}(x_d, z_d) = \mathbf{G}\, \Delta \mathbf{m}(x_a, z_a) . \tag{3.1}$$

One complication is immediately apparent. The migration slowness data $s(y_d, \tau_d)$, are a function of the midpoint y and migrated time τ, and not directly of the physical position (x_d, z_d). Hence one needs to know how to relate (x_d, z_d) to (y_d, τ_d). This suggests beginning with a model for which this map is known (such as a laterally invariant average background), and updating this map at each iteration by computing changes in the migrated location in time, $\Delta\tau_d$, and midpoint, Δy_d, as well as the change in migration slowness Δs_d. The operator $\mathbf{G}$ thus has three parts:

$$\begin{bmatrix} \Delta \mathbf{s}_d \\ \Delta \tau_d \\ \Delta \mathbf{y}_d \end{bmatrix} = \begin{bmatrix} \mathbf{G_s} \\ \mathbf{G}_\tau \\ \mathbf{G_y} \end{bmatrix} \Delta \mathbf{m} . \tag{3.2}$$

As I show later in this chapter, one also needs to incorporate information about local dips in the operator. This dip information can be estimated from the time

migrated image extracted from the constant-velocity prestack time migrations using the current estimate of the migration velocity function. These dips will be slopes in migrated time, so as the local estimate of the migration velocity s_d is updated, the conversion to physical dips will also change. Thus, at each iteration both the position (x_d, z_d) and the dip θ_d corresponding to a point (y_d, τ_d) in the time migrated data will change. In effect, one computes a mapping from a time-migrated image to a depth-migrated image as one iterates away from a laterally invariant velocity model to a laterally varying one, a mapping similar in effect to that found by tracing image rays (Larner et al., 1981).

3.3 FILTERED TOMOGRAPHY

The construction of the operator **G** can be split into two parts. The first part finds $\partial t / \partial m$ by tomography, and the second finds $\partial s / \partial t$, $\partial \tau / \partial t$, and $\partial y / \partial t$ by generalized inversion of double-square-root traveltime equations. The operator **G** thus decomposes into a tomographic operator **B**, and a filtering operator **A**:

$$\begin{bmatrix} \Delta \mathbf{s}_d \\ \Delta \boldsymbol{\tau}_d \\ \Delta \mathbf{y}_d \end{bmatrix} = \mathbf{A}\,\mathbf{B}\,\Delta\mathbf{m} \; . \tag{3.3}$$

The operator **A** that expresses the double-square-root traveltime equation perturbations is not found directly. Instead a forward operator **C** is found that relates traveltime changes Δt to perturbations in the parameters Δs_d, $\Delta \tau_d$, and Δy_d. Then $\mathbf{A}=\mathbf{C}^{-g}$, where the superscript $-g$ is used here to mean that **A** is a generalized inverse to **C**.

Relating model perturbations to traveltime perturbations

The computation of traveltimes to a subsurface point given a velocity model is done readily by ray tracing. For a ray R, the traveltime is just the integral along a ray of the slowness m:

$$t = \int_R m \; dr \tag{3.4}$$

where r is the arc length along the ray. Invoking Fermat's principle, one can perturb the model and calculate the changes in traveltimes integrating the slowness perturbations along the *unperturbed* ray R:

$$\Delta t = \int_R \Delta m \; dr = \mathbf{B}\,\Delta\mathbf{m} \; . \tag{3.5}$$

In discretized form, this gives a linear operator **B** relating interval slowness perturbations to travel time changes. For general background models, computation of **B** requires tracing rays; for a constant slowness background, this operator can be found analytically. This is a standard computation for a tomographic inversion. However, rather than pick traveltimes and try to invert **B** to find interval velocities, I use the migration-velocity filter **A** so that events never need to be picked explicitly, which should be a boon in noisy or complicated data.

Relating traveltime perturbations to diffraction pyramids

Consider first a single point diffractor at $\mathbf{d}=(x_d, z_d)$ in a medium of constant slowness s. If one runs a seismic survey passing over this point, the kinematics of the pre-stack point diffractor are described by the equation

$$t = s\sqrt{z_d^2+(y-h-x_d)^2} + s\sqrt{z_d^2+(y+h-x_d)^2} \tag{3.6}$$

where t, y, and h are the traveltime, the midpoint, and the half-offset specifying an event in a particular trace. In a space with midpoint, offset, and time as coordinates, this equation describes a pyramidal surface with rounded corners, as illustrated in Figure 3.1. This pyramid is the summation surface for a Kirchhoff integral formulation of prestack time migration; it is the generalization to non-zero offsets of the hyperbolic diffraction surface used for zero-offset migration. The migration slowness describes the curvature of this pyramid, that is, how flat or peaked it appears.

Suppose now that the slowness model is perturbed. The travel-time data for the point diffractor, $\{t_{ik}, y_i, h_k\}$, no longer satisfy equation (3.1) exactly. However, if the perturbations are not too large, there exist a slowness s_d, a zero-offset time τ_d, and a lateral position y_d for which an equation of the form

$$t = \sqrt{\tau_d^2/4 + s_d^2(y-h-y_d)^2} + \sqrt{\tau_d^2/4 + s_d^2(y+h-y_d)^2} \tag{3.7}$$

best fits the data points in a least-squares sense.

One can solve the problem of fitting such a pyramid through the data points $\{t_{ik}, y_i, h_k\}$ by linearizing around an initial value of $(\hat{s}_d, \hat{\tau}_d, \hat{y}_d)$. One gets the set of equations

$$\Delta t(y_i, h_k) = t_{ik} - t(\hat{s}_d, \hat{\tau}_d, \hat{y}_d) \approx \frac{\partial t}{\partial s_d}\Delta s_d + \frac{\partial t}{\partial \tau_d}\Delta \tau_d + \frac{\partial t}{\partial y_d}\Delta y_d \tag{3.8}$$

where all the partial derivatives are evaluated at $(\hat{s}_d, \hat{\tau}_d, \hat{y}_d, y_i, h_k)$; there will be one equation for each midpoint-offset pair. Written as a matrix equation, this becomes

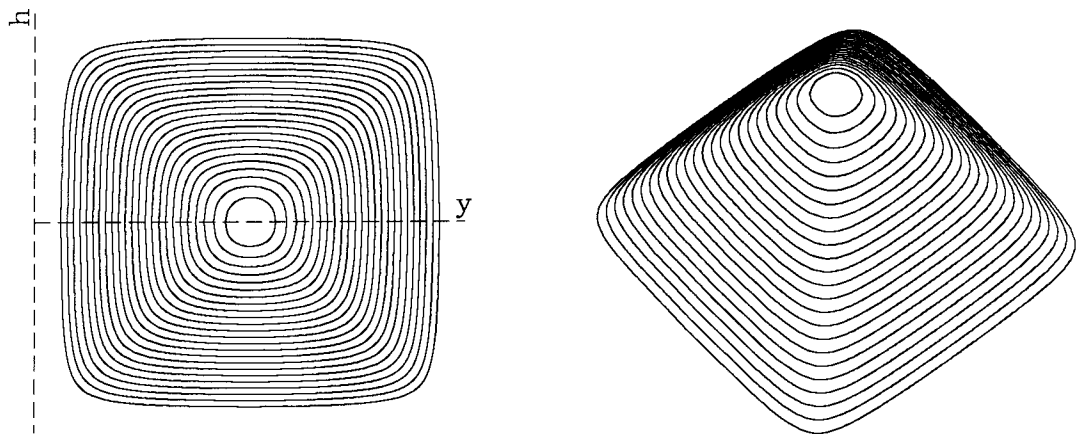

FIG. 3.1. Pyramidal traveltime surface for a point diffractor in prestack data. The coordinates are midpoint y, offset h, and traveltime t. Contours are curves of equal traveltime. On the left is a view looking vertically down the t axis. On the right is an oblique view. These pictures schematically illustrate equation (3.6). The migrated time τ and midpoint y define the location of the apex of the pyramid. The migration slowness s controls the curvature, or how broad or peaked the pyramid is.

$$\Delta \mathbf{t} \approx \mathbf{C} \begin{bmatrix} \Delta \mathbf{s}_d \\ \Delta \tau_d \\ \Delta \mathbf{y}_d \end{bmatrix} \tag{3.9}$$

where $\mathbf{C}$ is a matrix of the partial derivatives of t. Letting $\mathbf{A} \equiv \mathbf{C}^{-g}$ be a generalized inverse for $\mathbf{C}$, one can write

$$\begin{bmatrix} \Delta \mathbf{s}_d \\ \Delta \tau_d \\ \Delta \mathbf{y}_d \end{bmatrix} = \mathbf{C}^{-g} \, \Delta \mathbf{t} = \mathbf{A} \, \Delta \mathbf{t} = \mathbf{A} \, \mathbf{B} \, \Delta \mathbf{m} \tag{3.10}$$

which is just the desired decomposition of $\mathbf{G}$.

If this generalized inverse is taken in the usual least-squares sense (see, e.g., Menke, 1984), the normal equations can be solved explicitly. Toldi (1985) used an explicit solution of this form for stacking velocities, and I use one simple case of an explicit solution to equation (3.10) in section 3.8 to show how to derive Toldi's operator for flat dips from the more general one presented here. For the general operator, however, the computation of an explicit closed form solution becomes too complicated to be useful. Moreover, the explicit solution will be unstable for reasons I

discuss in section 3.7. I use singular value decomposition (SVD) to give a stable inverse, zeroing singular values that are too close to zero. Because there are only three singular values here, the computational cost of SVD is minimal.

The least-squares fitting in the inversion of **C** to find **A** can incorporate an arbitrary weighting of the different rows in equation (3.9). I know of no strong theoretical motivation for favoring any particular weighting. In section 3.8 I show that Toldi's approach is equivalent to using weighting proportional to the total traveltime, because of his use of a transformation to t^2–h^2 coordinates in defining the least-squares inverse. In practice I have usually used a weighting for even sampling in angle rather than in offset, as I discuss further in section 3.6. Numerical testing suggests that the choice of weights has only a small effect on the result.

3.4 COMPUTING THE GENERAL OPERATOR

To see how G is computed, let

$$\mathbf{A} = \mathbf{C}^{-g} = \begin{bmatrix} \mathbf{A}_s \\ \mathbf{A}_r \\ \mathbf{A}_y \end{bmatrix}. \tag{3.11}$$

A specific set of rays corresponding to particular choices of midpoint and offset sampling are used in defining **C**, and hence in finding **A**. In general, if one specifies a subsurface reflector point **d** and an anomaly point **a** at which the velocity is to be perturbed, the rays that pass through this velocity anomaly and reflect from the specified point **d** will not be part of the set used in defining **C**. This is not a problem, however, because once the inverse operator **A** has been found for a specified set of values of y and h, interpolation can be used to calculate the operator anywhere other than at the original sampling points, as long as the anomalous ray is within the aperture limits set by the extreme values used in the initial fitting. In effect, the back-projection is weighted by a set of coefficients that implicitly interpolates onto whatever grid points are needed.

Figure 3.2 shows the geometry of the ray path for a particular diffractor point, midpoint, and offset in an arbitrary velocity model. Let the subscript d refer to the coordinates of a particular diffractor point $\mathbf{d}\equiv(x_d, z_d)$, and let the subscript a refer to the location of a slowness anomaly $\mathbf{a}\equiv(x_a, z_a)$, that is, a particular element of the model **m**. Such an anomaly at a depth z_a can affect the diffraction pyramid if it is at either of two positions x_a, since it can be intercepted by either the ray going down or the one coming back up. Using the notation of Figure 3.2, equation (3.5)

becomes

$$\Delta t_{ik} = \int_{z_a} dz_a \int_{x_a} dx_a \, \Delta m\,(x_a\,,z_a\,)\left(\frac{\delta_1}{\cos\psi_{ik}\,(z_a\,)} + \frac{\delta_2}{\cos\phi_{ik}\,(z_a\,)} \right) \tag{3.12}$$

where the delta functions δ_1 and δ_2 are defined by

$$\delta_1 \equiv \delta[x_a - y'_i\,(z_a\,) + \mu_{ik}\,(z_a\,)] \tag{3.13}$$

and

$$\delta_2 \equiv \delta[x_a - y'_i\,(z_a\,) - \nu_{ik}\,(z_a\,)] \; . \tag{3.14}$$

These delta functions pick out the values of the anomaly locations $(x_d\,,z_d\,)$ that lie on a particular ray. The parameters μ and ν are the effective offsets of the two legs of the ray path at each depth; they are measured from the point $y'(z_a\,)$ on the zero-offset ray. The angles ψ and ϕ are the ray directions at the anomaly depth. The cosine factors are introduced to convert from integration along the ray itself to integration over the depth z_a. Because most rays in reflection experiments are more nearly vertical than horizontal, it is natural to use an integral over z_a rather than one over the lateral position x_a. In converting to such an integral, however, I implicitly rule out the use of turning rays in the computations that follow.

Now assume that a rule is known associating a diffracting point $(x_d\,,z_d\,)$ with the point $(y_d\,,\tau_d\,)$ where it appears in the data. Looking first at Δs_d, one can write equation (3.10) as

$$\Delta s_d\,(y_d\,,\tau_d\,) = \sum_i \sum_k (A_s\,)_{ik}\, \Delta t_{ik} \tag{3.15}$$

and substitute from equation (3.12) for Δt_{ik} to yield

$$\Delta s_d\,(y_d\,,\tau_d\,) = \sum_i \sum_k (A_s\,)_{ik} \int_{z_a} dz_a \int_{x_a} dx_a \, \Delta m\,(x_a\,,z_a\,) \times \left(\frac{\delta_1}{\cos\psi_{ik}\,(z_a\,)} + \frac{\delta_2}{\cos\phi_{ik}\,(z_a\,)} \right) . \tag{3.16}$$

Pull the integrals outside the sums to get

$$\Delta s\,(\mathbf{d}) = \int_{z_a} dz_a \int_{x_a} dx_a \; G_s\,(\mathbf{d},\mathbf{a}) \Delta m\,(x_a\,,z_a\,) \tag{3.17}$$

where

$$G_s\,(\mathbf{d},\mathbf{a}) = \sum_{i=1}^{N_y} \sum_{k=1}^{N_k} (A_s\,)_{ik} \left(\frac{\delta_1}{\cos\psi_{ik}\,(z_a\,)} + \frac{\delta_2}{\cos\phi_{ik}\,(z_a\,)} \right) . \tag{3.18}$$

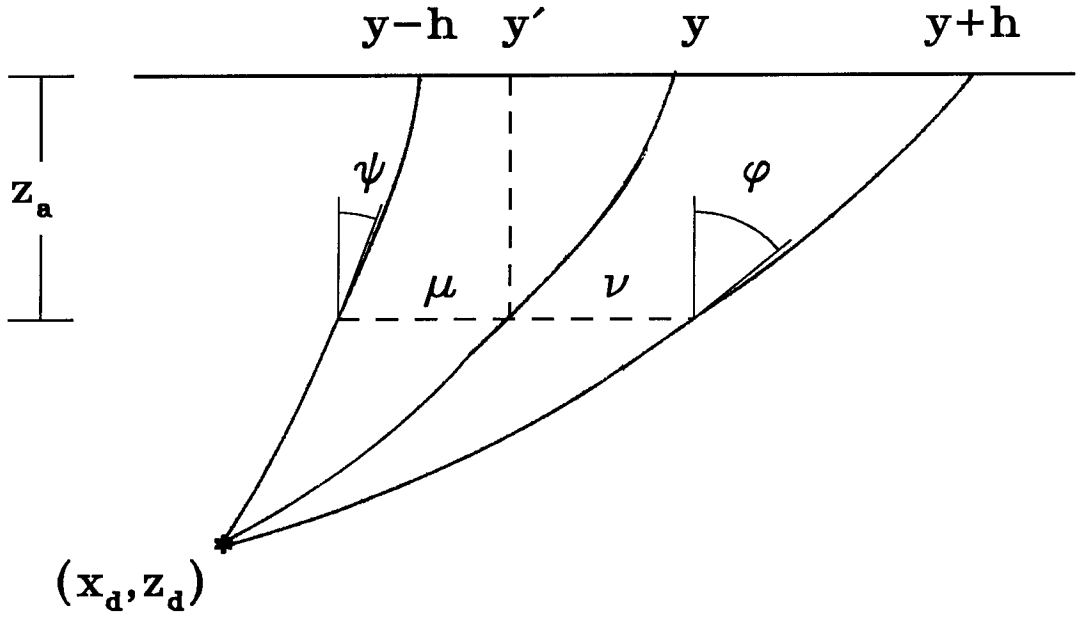

FIG. 3.2. Geometry of rays for a single diffractor point and a variable background slowness. The rays for a single trace with midpoint y and offset h are shown, along with the zero-offset ray. The diffractor is at (x_d, z_d). The point in the model at which the slowness is perturbed is at depth z_a. The quantities ϕ, ψ, μ, ν and y' are used in calculating the effect on the travel-time of perturbing the slowness.

Now the linear operator is written explicitly as an integral with a Green function kernel. This Green function $G_s(\mathbf{d},\mathbf{a})$ can be identified with $\partial s_d / \partial m_a$; they both represent the change in $s(y,\tau)$ caused by a perturbation in $m(x,z)$. One can also write similar Green function representations for $G_\tau(\mathbf{d},\mathbf{a}) = \partial \tau_d / \partial m_a$ and for $G_y(\mathbf{d},\mathbf{a}) = \partial y_d / \partial m_a$ simply by substituting A_τ or A_y in place of A_s in equation (3.18).

Evaluation of the Green function $\mathbf{G}_s$ against a general background velocity model requires tracing rays for each diffractor and each midpoint y and offset h. Once the ray paths are known, the various values of μ, ν, y', ϕ, and ψ can be computed. Note that the delta functions were introduced in equation (3.12) to pick out those values of x_a and z_a that fall on a specified ray. In evaluating the Green function the role of the delta functions is turned around: it is assumed that the slowness anomaly location **a** is known, and the delta functions are now used to pick out the ray from the reflecting point **d** to the surface that passes through **a**.

Consider first the sum containing δ_1,

$$(G_s)_1(\mathbf{d},\mathbf{a}) = \sum_{i=1}^{N_y}\sum_{k=1}^{N_h} \frac{A_s(y_i,h_k)\delta_1}{\cos\psi_{ik}(z_a)} \tag{3.19}$$

$$= \sum_{i=1}^{N_y}\sum_{k=1}^{N_h} \frac{A_s(y_i,h_k)\,\delta[x_a - y'_i(z_a)+\mu_{ik}(z_a)]}{\cos\psi_{ik}(z_a)} \,. \tag{3.20}$$

Note that for $z_a = 0$, one has $\mu_{ik} = h_k$ and $y_i' = y_i$. The delta function was defined to pick out a particular x_a for a specified z_a. Now I want to change variables so that it picks out a particular value of the offset h corresponding to the ray through **a**. Let γ be the relative offset at depth z_a compared to the surface offset h_k, that is,

$$\gamma(y_i,h_k,z_a) = \frac{h_k}{\mu_{ik}(z_a)} \,. \tag{3.21}$$

At zero offset, this expression becomes formally undefined, and must be evaluated as a limit. This is not a significant problem, because the limit is well behaved and γ is continuous approaching zero offset; the apparent ambiguity is caused simply by the choice of variables. In Appendix B, I show how to compute $\gamma(h=0)$.

Changing variables in the delta function then gives

$$\delta[x_a - y'_i(z_a)+\mu_{ik}(z_a)] = \gamma(y_i,h_k,z_a)\,\delta\Big(\gamma(y_i,h_k,z_a)\,[x_a - y'_i(z_a)] + h_k\Big) \,. \tag{3.22}$$

Now approximate the sum over h_k as an integral, and use the delta function to eliminate it. Let Δh be the survey offset spacing. Then

$$(G_s)_1(\mathbf{d},\mathbf{a}) = \sum_{i=1}^{N_y} \frac{1}{\Delta h}\int dh \frac{A_s(y_i,h)\,\gamma(y_i,h,z_a)}{\cos\psi_i(h,z_a)}\,\delta\Big(\gamma(y_i,h,z_a)[x_a - y'_i(z_a)]+h\Big) \tag{3.23}$$

For a specified midpoint y_i, let h_i be the particular value of h corresponding to the ray from **d** through **a**. (Note the change in subscript from k to i.) The value of h_i can be found by tracing rays. The delta function zeroes out all other values of h, so that

$$h_i = -\gamma(y_i,h_i,z_a)\Big[x_a - y'_i(z_a)\Big] \tag{3.24}$$

or

$$\gamma(y_i,h_i,z_a) = \frac{-h_i}{\Big[x_a - y'_i(z_a)\Big]} \,. \tag{3.25}$$

Then

$$(G_s)_1(\mathbf{d},\mathbf{a}) = \frac{1}{\Delta h}\sum_{i=1}^{N_y}\frac{A_s(y_i,h_i)\,\gamma(y_i,h_i,z_a)}{\cos\psi_i(h_i,z_a)} \tag{3.26}$$

$$= \frac{1}{\Delta h}\sum_{i=1}^{N_y}\frac{-h_i\;A_s(y_i,h_i)}{\left[x_a - y'_i(z_a)\right]\cos\psi_i(h_i,z_a)}\,. \tag{3.27}$$

A similar argument can be used to compute $(G_s)_2(\mathbf{d},\mathbf{a})$, corresponding to the other leg of the ray path. The resulting expression becomes

$$(G_s)_2(\mathbf{d},\mathbf{a}) = \frac{1}{\Delta h}\sum_{i=1}^{N_y}\frac{h_i\;A_s(y_i,h_i)}{\left[x_a - y'_i(z_a)\right]\cos\phi_i(h_i,z_a)}\,. \tag{3.28}$$

Equation (3.28) is equivalent to equation (3.25) with $-h_i$ substituted for h_i, that is, to the reciprocal experiment with shot and receiver locations interchanged. (Note that $A(y_i,-h_i)=A(y_i,h_i)$, and that the meanings of the angles ψ and ϕ will be interchanged as well, since the identification of the downgoing and upcoming legs of the ray path are reversed.) Because I now am assuming that $\mathbf{a}$ is known, the separate delta functions for the two legs of the ray path are redundant. Including both terms corresponds to including the reciprocal experiment which, since only the kinematics of isotropic P-waves are being considered, contains no additional information. Hence I can always take h_i to be positive and write the complete operator simply as

$$G_s(\mathbf{d},\mathbf{a}) = \frac{1}{\Delta h}\sum_{i=1}^{N_y}\frac{h_i\;A_s(y_i,h_i)}{\left|x_a - y_i'(z_a)\right|\cos\psi_i(h_i,z_a)} \tag{3.29}$$

where now I use ψ to indicate the ray angle at $\mathbf{a}$ regardless of which leg is being considered.

Thus, computing the operator $G_s(\mathbf{d},\mathbf{a})$ requires tracing two rays from $\mathbf{d}$ for each midpoint y_i: the zero offset ray to the surface point $(y_i,0)$, and the ray that passes through $\mathbf{a}$. One needs to find from these rays the surface offset h_i, the effective offset $x_a - y_i'(z_a)$ at depth z_a, and the ray angle $\cos\psi_i$ at $\mathbf{a}$. These computations are greatly simplified for a laterally invariant background, since the operator is then convolutional in the lateral direction x; the ray tracing becomes identical for all midpoints and need only be done once. Note that a rule for finding (y_d,τ_d) as a function of (x_d,z_d) is also needed, and that this rule too is greatly simplified for a laterally invariant background. The whole computation of $\mathbf{G}_s$ is even easier for a constant background, and may be done analytically in that simple case, as I discuss

in section 3.6.

3.5 WEIGHTING DIPS SELECTIVELY: THE DIP-DEPENDENT OPERATOR

So far I have derived an expression for $\partial s / \partial m$ for a point diffractor. In a constant velocity medium the migration slowness is independent of structure, so the value of migration slowness measured for a point diffractor is the same as that measured for any structure. This does not guarantee, however, that $\partial s / \partial m$ is also structure independent; in fact it depends on the reflector dip. One does not normally see pyramidal traveltime surfaces in seismic data. Discrete point diffractors are rare; reflections from continuous beds usually dominate the data. These continuous reflections can be built up mathematically as a limiting sum of many point diffractions; constructive and destructive interference of the waves results in the continuous events one observes. Similarly, in migration, when summing over the entire traveltime pyramid, one is implicitly back-propagating waves, and treating each point as an isolated diffractor. Here, however, one is *back-projecting* traveltimes rather than *back-propagating* waves, and no wave interference effects occur. Hence one has to introduce explicit information about the continuity of reflectors in the form of knowledge of dips. Rather than considering rays corresponding to all midpoints and offsets, one has to single out those rays that obey the simple rule from geometrical optics that incident angles must equal reflected angles; these will be the only rays that carry significant energy.

Suppose the reflecting point **d** lies on a bed with dip θ. Figure 3.3 shows the geometry of rays reflecting off such a dipping bed. Unlike the rays used for stacking-velocity analysis, the rays for migration-velocity analysis have a common reflection point, and (barring caustics caused by the velocity field) do not cross each other. Note that the ray picture for migration-velocity analysis is like that for flat-bed stacking-velocity analysis, but rotated by the dip angle so that the rays remain symmetric around the normal incidence ray.

Each point diffractor can be treated as made up equally of all dips. Limiting the point diffractor Green function to a single dip component thus has the effect of zeroing out all but a particular value of y in the sum of equation (3.29). This corresponds to selecting the one ray that passes through the anomaly **a** and has equal incident and reflected angles at the point **d** on a bed with dip θ. Write the values of midpoint and offset that describe this unique geometrical optics ray as h_θ and y_θ. Equation (3.29) then becomes

$$(G_s)_\theta(\mathbf{d},\mathbf{a}) = \frac{h_\theta \, A_s(y_\theta, h_\theta)}{\Delta h \left| x_a - y'_\theta(z_a) \right| \cos\phi_\theta(z_a)} \, . \tag{3.30}$$

The different terms in equation (3.30) can each be understood easily. A_s comes from the least-squares fitting of traveltimes to a diffraction pyramid, and it is evaluated at the point corresponding to the unique geometrical optics ray. The factor of $h / | x_a - y'_\theta(z_a) |$ is the normalized cable aperture at depth z_a, and acts as a weight to allow for increasing ray density in the fan of rays from the subsurface point **d** to the surface. If the slowness anomalies are assigned to cells of equal size, a cell closer to **d** will be traversed by more rays in this fan than a shallower cell would be, and so should be weighted more heavily. The factor of Δh arises from using a discrete sampling in offset h. Increasing the number of offsets within a given offset range increases the ray density accordingly, causing more rays to traverse a given slowness anomaly cell, and so G_s must be scaled accordingly. Finally, the cosine factor arises from treating the rays as parametrized by the depth z_a; the cosine converts from the vertical distance to the arc length for a ray that is not traveling vertically. In summary, $(G_s)_\theta$ is just A_s weighted by terms that arise from the ray geometry and the model parametrization.

A subtle, but important, point to notice here is that A_s in the equation (3.30) should really be written as $(A_s)_\theta$, since A_s will in fact now be different for each dip. The least squares fitting used in the inversion of **C** to get **A** must also be taken only over the constant velocity geometrical optics rays, which differ for each dip, rather than over the whole pyramid. The traveltime pyramid can be decomposed into components corresponding to different dips. Then, instead of finding a best fitting diffraction pyramid, only the particular part of the pyramid that corresponds to the single dip θ is fitted. Figure 3.4 shows a pyramid decomposed into dip components; the heavy solid lines show the (y, h, t) curves for various dips. These curves are generalizations of hyperbolic NMO stacking curves that define the effective summation paths for prestack time migration. Standard NMO stacking sums data for all offsets at a fixed midpoint; this is the hyperbolic moveout curve corresponding to flat dip in Figure 3.4. For dips other than zero, the summation is along one of the generalized moveout curves in both midpoint y as well as offset h. Prestack migration actually always sums over the entire pyramid, but if only one dip is present, only data along the corresponding generalized stacking curve contributes constructively to the migrated image.

In Appendix C, I derive equations describing this decomposition of the traveltime pyramid into the contributions corresponding to different dips. The midpoints y and offsets h that represent valid rays for a given dip θ and a constant velocity background must satisfy

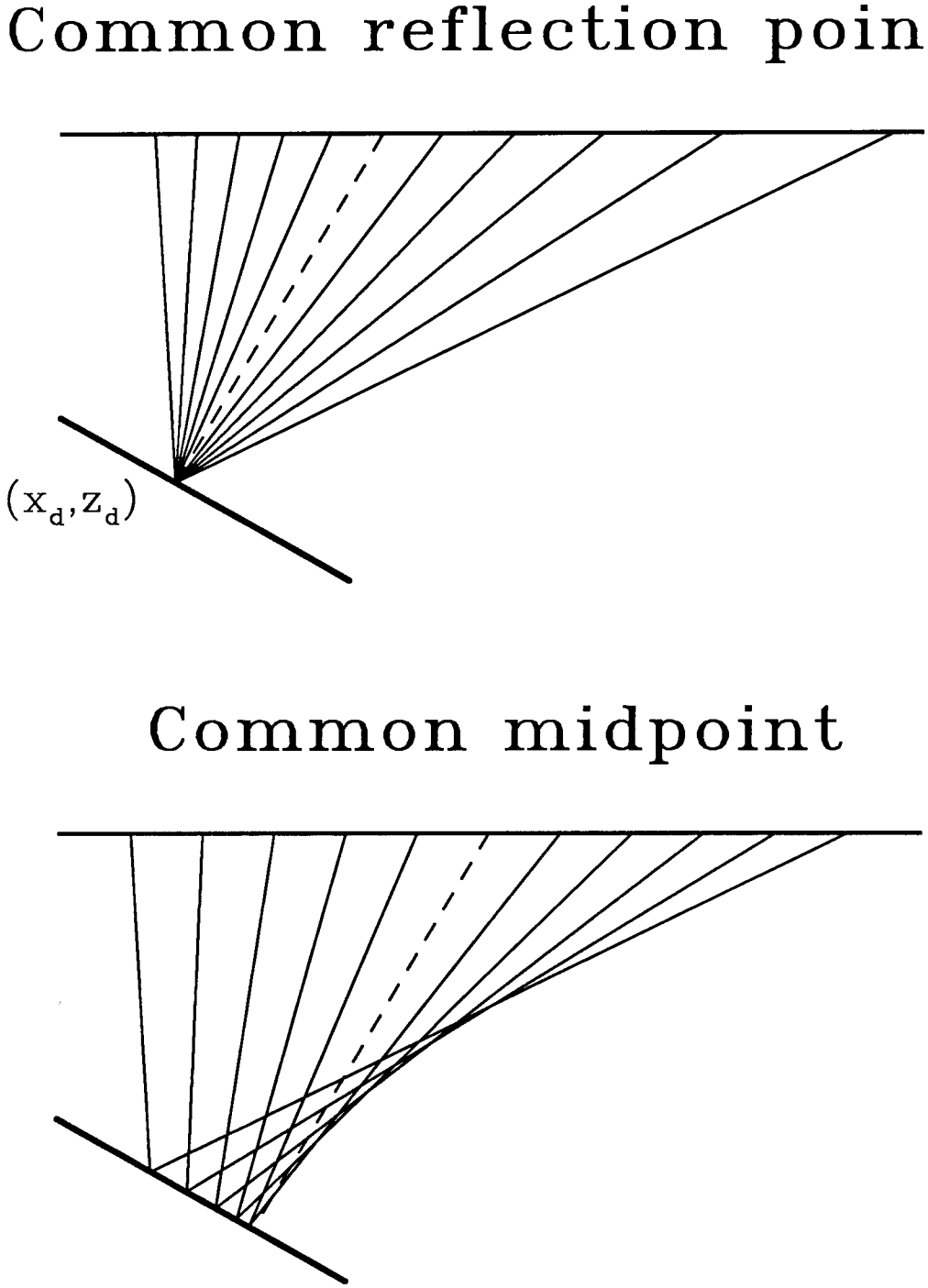

FIG. 3.3. Geometry of rays for a dipping bed and a constant background slowness. The upper picture shows a common-reflection point gather, with rays for various incident angles. The reflecting point is at (x_d, z_d). The lower picture shows a common-midpoint gather, with rays for traces with a single midpoint and various offsets h. Note that in the first picture, midpoint changes with offset, whereas in the second, the reflection point moves with offset. The zero-offset ray is shown as a dashed line in both pictures.

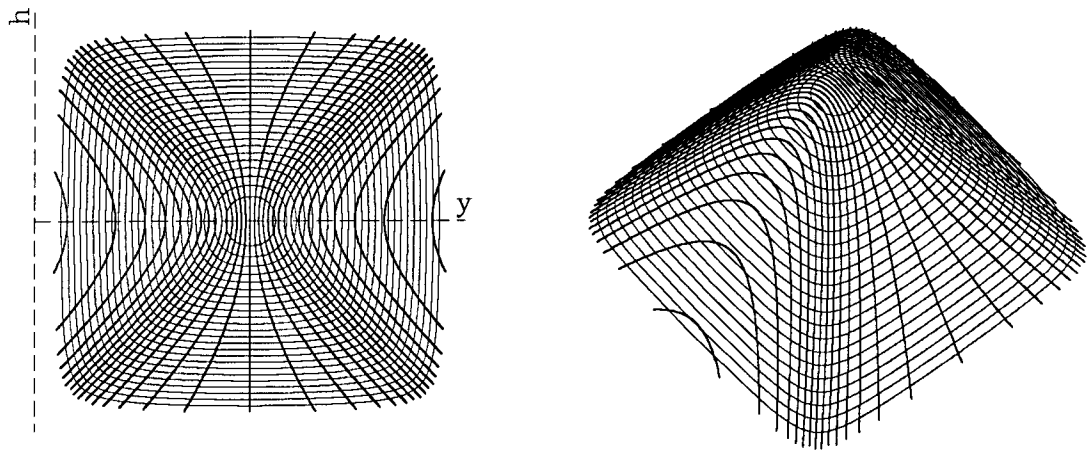

FIG. 3.4. Dip-decomposition of a pyramidal traveltime surface for a point diffractor in prestack data. The coordinates are midpoint y, offset h, and traveltime t. Light contours are curves of equal traveltime. On the left is a view looking vertically down the t axis. On the right is an oblique view. Heavy lines represent constant dip contributions, in increments of 5 degrees.

$$\tan(2\theta) = \frac{2z_d\,(y-x_z)}{z_d{}^2-(y-x_d)^2+h^2} \quad . \tag{3.31}$$

These dip component curves, projected into the (y,h) plane, are hyperbolas, as shown in the vertical view of a traveltime pyramid in Figure 3.4. Flat dip is the limiting case in which the hyperbola becomes a straight line, with $h=0$ and $y=x_d$. Note that these curves are *not* the same as the hyperbolas seen in radial trace sections (Claerbout, 1985); these moveout curves are not hyperbolas, although their projections in (y,h) are. Moreover, even the hyperbolic projections are generally not centered around x_d.

What does this mean in practice? It suggests that the operator should be weighted to reflect the dips actually present in the data at each point. For the case of a single dip component, these weights are just delta functions that would pick out the contour representing a given dip, and are zero elsewhere. In practice, one might weight by an estimate of the dips in the data, allowing for multiple dips and

inaccurate knowledge of the dips. Reasonable dip estimates can be obtained from the migrated image using local slant stacks. The $\mathbf{G}_s$ operator can then be weighted by this estimated dip spectrum. Picking a single dominant dip at each point corresponds to the usual practice in tomographic inversion of digitizing horizons; using a weighted spectrum of dips "blurs" the back-projection, allowing for the uncertainty with which one can really determine dips from data. These dips will be slopes in migrated time so, as the local estimate of the migration velocity s_d is updated, the conversion to physical dips will also have to be updated. Thus, at each step of an iterative, nonlinear inversion, the dip θ_d as well as the position (x_d, z_d) corresponding to a point (y_d, τ_d) in the time-migrated data will change.

Finally, note that the above discussion concerned only $\mathbf{G}_s$ but the complete operator is tripartite, as developed in section 3.2. The extension of equation (3.30) is straightforward, however. The entire derivation is the same for $\mathbf{G}_\tau$ and $\mathbf{G}_y$, with equivalent expressions obtained simply be replacing A_s in equation (3.30) by A_τ and A_y, respectively.

3.6 THE LINEAR OPERATOR FOR CONSTANT SLOWNESS BACKGROUND

The case of constant slowness background is particularly useful for understanding the behavior of the $\mathbf{G}$ operator. If the background slowness model is constant the rays in Figure 3.2 are straight, ϕ and ψ become independent of z_a, and $\mu=\nu$. As argued in section 3.4, I can use either leg of the ray path in computing G_s; I choose the left-hand leg in Figure 3.2. Explicitly,

$$\gamma = \frac{h}{\mu} = \frac{h}{y'-x_a} = \frac{z_d}{z_d-z_a} \; . \tag{3.32}$$

The last equality is derived using similar triangles. As defined in equation (3.25), γ normally depends on the midpoint y_i, but here γ is independent of which y_i is being considered, and depends only on z_a and z_d. Another application of similar triangles shows that

$$y-h-x_d \; = \gamma(x_a-x_d) \; . \tag{3.33}$$

From this, one also has that

$$\cos\psi = z_d \; \left[z_d{}^2+(y-h-x_d)^2 \right]^{-1/2} \tag{3.34}$$

$$= z_d \; \left[z_d{}^2+\gamma^2(x_a-x_d)^2 \right]^{-1/2} \; . \tag{3.35}$$

Making these substitutions into equation (3.29) yields

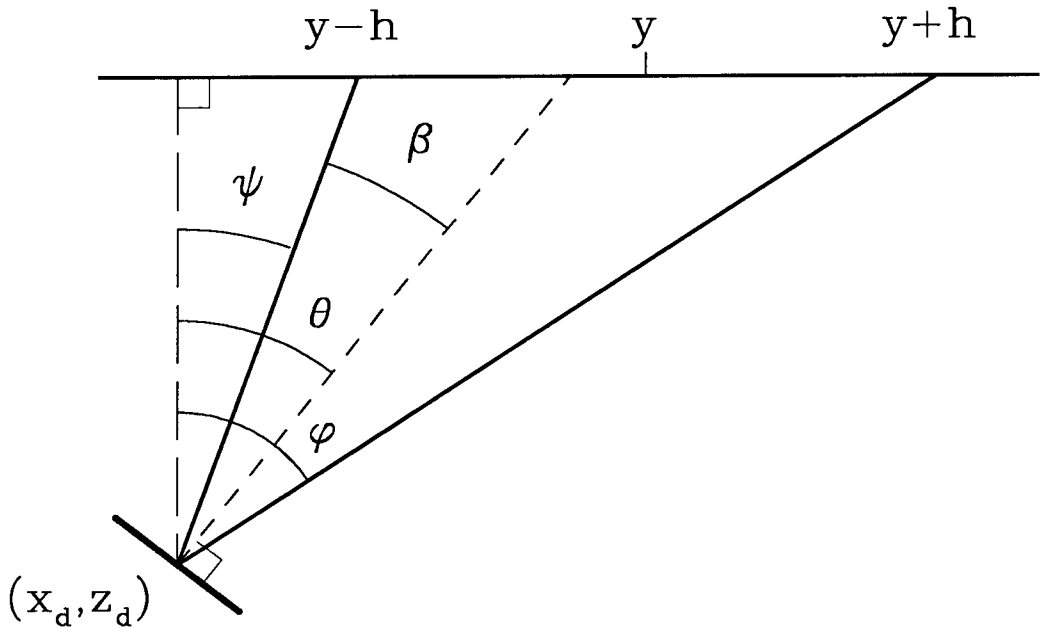

FIG. 3.5. Geometry of rays for a dipping bed and a constant background slowness. The rays for a single trace with midpoint y and offset h are shown, along with the normal ray (dashed). The reflecting point is at (x_d, z_d). Note that the normal ray does not go through y.

$$G_s(\mathbf{d},\mathbf{a}) = \frac{\gamma}{z_d \Delta h} \left[z_d^2 + \gamma^2 (x_a - x_d)^2 \right]^{1/2} \sum_{i=1}^{N_y} A_s(y_i, \mid h_i \mid) \tag{3.36}$$

where h_i can be found from equation (3.34). The single dip operator can be found similarly by substituting into equation (3.30) to get

$$G_s(\mathbf{d},\mathbf{a}) = \frac{\gamma}{z_d \Delta h} \left[z_d^2 + \gamma^2 (x_a - x_d)^2 \right]^{1/2} A_s(y_\theta, \mid h_\theta \mid) . \tag{3.37}$$

The explicit values of y_θ and h_θ are

$$y_\theta = x_d + \frac{z_d^2 + \gamma^2 (x_a - x_d)^2}{2[z_d \cot 2\theta + \gamma (x_a - x_d)]} \tag{3.38}$$

and

$$h_\theta = \left| \frac{z_d^2 + \gamma^2 (x_a - x_d)^2}{2[z_d \cot 2\theta + \gamma (x_a - x_d)]} - \gamma (x_a - x_d) \right| . \tag{3.39}$$

For a derivation of these last equations, see Appendix C.

The y and h in the above equations will now usually not fall on grid points, but A can be calculated for any y or h numerically, as discussed in section 3.4. In all these computations against a constant-slowness background, one can use $(\tau_d, y_d) = (2sz_d, x_d)$ if an explicit relation between $\Delta s(y_d, \tau_d)$ and $\Delta s(x_d, z_d)$ is needed.

The constant velocity single dip case can provide useful insight into weighting schemes to be used. First, as mentioned in section 3.3, the least squares inversion of **C** to get **A** can include an arbitrary set of weights. Computation of the full **G** operator requires tracing a set of rays from the point **d** to the surface, which is easiest if done in equal angular increments away from normal incidence at the bed. Call this angle between the two legs of the ray path β, as indicated in Figure 3.5. Then it is natural to weight the fitting over offset h by $\partial\beta/\partial h$ to make the fitting equivalent to one over the angle β. The value of this derivative is also calculated in Appendix C; the result is given by

$$\frac{\partial\beta}{\partial h} = \frac{z_d\ (z_d^2+(y-x_d)^2+h^2)}{[\ z_d^2-(y-x_d)^2+h^2\ ]^2+4z_d^2(y-x_d)^2} \tag{3.40}$$

$$= \frac{z_d\ (z_d^2+(y-x_d)^2+h^2)}{[\ z_d^2+(y-x_d)^2+h^2\ ]^2-4(y-x_d)^2h^2}\ . \tag{3.41}$$

These are the weights I have used in all the examples that follow, except in the comparison with Toldi's operator in section 3.8. However, as mentioned in section 3.4, numerical testing suggests that the behavior of the operator is insensitive to the choice of these weights.

One can combine the operators for all dips and write

$$G_s(\mathbf{d},\mathbf{a}) = \int d\,\theta\ \varsigma_\theta(\mathbf{d})\ (G_s)_\theta(\mathbf{d},\mathbf{a}) \tag{3.42}$$

where ς represents weights corresponding to the estimated dip spectrum at **d**. The multi-dip operator was originally formulated in equation (3.29) as a sum over midpoint y instead of angle θ. If one were to implement it this way it would be natural not to favor one dip over another, and hence to weight the sum (or integral) over y by $\partial\theta/\partial y$. The value of $\partial\theta/\partial y$ for the constant velocity background is derived in Appendix C; it is identical to $\partial\beta/\partial h$ as given in equations (3.40) and (3.41).

3.7 A DEGENERATE DEGREE OF FREEDOM

In implementing the single-dip constant-slowness operator, I found that the matrix **C** was persistently singular. Singular value decomposition of **C** showed that there was always one singular value that was far smaller than the other two, suggesting that only two of the parameters Δs_d, $\Delta \tau_d$, and Δy_d could be found independently. For the flat bed, this may be understood readily. Explicitly, the derivatives in equation (3.8) are given by

$$\begin{bmatrix} t_{s_d} \\ t_{\tau_d} \\ t_{y_d} \end{bmatrix} = \frac{1}{\sqrt{\tau_d^2/4 + s_d^2(y-h-y_d)^2}} \begin{bmatrix} s_d(y-h-y_d)^2 \\ \tau_d/4 \\ s_d^2(y_d-y+h) \end{bmatrix} + \frac{1}{\sqrt{\tau_d^2/4 + s_d^2(y+h-y_d)^2}} \begin{bmatrix} s_d(y+h-y_d)^2 \\ \tau_d/4 \\ s_d^2(y_d-y-h) \end{bmatrix} \tag{3.43}$$

where, to make the notation more compact, I denote the partial derivatives by subscripts: $\partial t/\partial s_d \equiv t_{s_d}$, etc. But for flat beds, $y = y_d$ always, and t_{y_d} is identically zero, so there are only two, not three, independent parameters to be found; hence **C** will be singular.

Why is **C** also singular for non-zero dips? Intuitively, the ray picture for migration-velocity analysis (the common reflection point gather in Figure 3.3) looks like that for flat-bed stacking-velocity analysis, but rotated by the dip angle so that the rays remain symmetric around the normal incidence ray. For flat dips one can resolve changes in τ_d, that is, vertical changes, but not changes in y_d horizontally along the bed. For the dipping bed it is reasonable to expect that one can similarly resolve changes perpendicular to the bed, but not parallel to it. Specifying a fixed dip angle θ eliminates one degree of freedom in the fitting function and makes it translationally invariant along the dip direction.

In terms of the angles ϕ, ψ, θ, and β in Figure 3.5, one has

$$\tan\psi = \frac{2s_d(y-h-y_d)}{\tau_d}, \tag{3.44}$$

$$\sin\psi = \frac{s_d(y-h)}{\sqrt{\tau_d^2/4 + s_d^2(y+h-y_d)^2}}, \tag{3.45}$$

and

$$\cos\psi = \frac{\tau_d}{2\sqrt{\tau_d^2/4 + s_d{}^2(y+h-y_d)^2}} \ . \tag{3.46}$$

The equations for ϕ are the same, with $y+h$ in place of $y-h$. In terms of these angles, the last two derivatives in equation (3.43) become

$$t_{\tau_d} = \frac{1}{2}(\cos\phi + \cos\psi) \tag{3.47}$$

$$= \frac{1}{2}\left[\ \cos(\theta-\beta) + \cos(\theta+\beta)\ \right] \tag{3.48}$$

$$= \cos\theta\,\cos\beta \tag{3.49}$$

and

$$t_{y_d} = -s_d\ (\sin\phi + \sin\psi) \tag{3.50}$$

$$= -s_d\left[\ \sin(\theta-\beta) + \sin(\theta+\beta)\ \right] \tag{3.51}$$

$$= -2s_d\ \sin\theta\,\cos\beta\ . \tag{3.52}$$

Thus, if θ is fixed,

$$\frac{t_{y_d}}{t_{\tau_d}} = -2s_d\tan\theta\ . \tag{3.53}$$

and so Δy_d and $\Delta\tau_d$ cannot be found independently. In practice, this means that, no matter what set of parameters is used, only two will be independent, and small singular values of $\mathbf{C}$ will need to be zeroed if three parameters are used in the inversion. Alternatively, $\mathbf{C}$ may be inverted in terms of only two variables, with the third found explicitly from these two.

3.8 THE FLAT-DIP OPERATOR

I now look in detail at the special case of θ=0. This operator should behave like Toldi's stacking operator, since for flat beds and laterally invariant velocities, prestack migration reduces to NMO stacking. All gathers will be symmetric, so $y_\theta = x_d$ and $h_\theta = |\ \gamma(x_a - x_d)\ |$, where γ is defined by equation (3.32). In terms of equation (3.43) this means that

$$\begin{bmatrix} t_{s_d} \\ t_{\tau_d} \\ t_{y_d} \end{bmatrix} = \frac{1}{\sqrt{\tau_d{}^2/4 + s_d{}^2h^2}} \begin{bmatrix} 2s_d\,h^2 \\ \tau_d/2 \\ 0 \end{bmatrix} . \tag{3.54}$$

So $t_{y_d}=0$, as one might expect.

To avoid cluttering the notation, I drop the subscript d on s, τ, and y for the rest of this section. Then the normal equations for solving equation (3.9) become

$$\begin{bmatrix} \mathbf{t_s}\cdot\Delta\mathbf{t} \\ \mathbf{t}_\tau\cdot\Delta\mathbf{t} \end{bmatrix} = \begin{bmatrix} \mathbf{t_s}\cdot\mathbf{t_s} & \mathbf{t}_\tau\cdot\mathbf{t_s} \\ \mathbf{t_s}\cdot\mathbf{t}_\tau & \mathbf{t}_\tau\cdot\mathbf{t}_\tau \end{bmatrix} \begin{bmatrix} \Delta s \\ \Delta\tau \end{bmatrix} \tag{3.55}$$

where I use inner product notation to denote the various sums, e.g.,

$$\mathbf{t_s}\cdot\mathbf{t}_\tau = \sum_{i,k} \alpha_{ik}\,(t_s)_{ik}\,(t_\tau)_{ik} \quad . \tag{3.56}$$

Here I explicitly include a set of weights α for the least-squares weighting. These normal equations (3.55) have a solution of the form

$$\begin{bmatrix} \Delta s \\ \Delta\tau \end{bmatrix} = \begin{bmatrix} \mathbf{A}_s\cdot\Delta\mathbf{t} \\ \mathbf{A}_\tau\cdot\Delta\mathbf{t} \end{bmatrix} \tag{3.57}$$

where

$$\mathbf{A}_s = \frac{1}{D}\left[(\mathbf{t}_\tau\cdot\mathbf{t}_\tau)\,\mathbf{t_s} - (\mathbf{t_s}\cdot\mathbf{t}_\tau)\,\mathbf{t}_\tau\right] \tag{3.58}$$

$$\mathbf{A}_\tau = \frac{1}{D}\left[-(\mathbf{t_s}\cdot\mathbf{t}_\tau)\,\mathbf{t_s} + (\mathbf{t_s}\cdot\mathbf{t_s})\,\mathbf{t}_\tau\right] \tag{3.59}$$

and

$$D = (\mathbf{t_s}\cdot\mathbf{t_s})\,(\mathbf{t}_\tau\cdot\mathbf{t}_\tau) - (\mathbf{t_s}\cdot\mathbf{t}_\tau)^2 \,. \tag{3.60}$$

For flat dip and a constant slowness background $y_d=x_d$, $s_d=s$, and $\tau_d=2sz_d$, and the various sums are over offset h only. Then

$$\mathbf{t_s}\cdot\mathbf{t}_\tau = \sum_h \alpha(y=x_d,h)\;t_s(y=x_d,h)\;t_\tau(y=x_d,h) \tag{3.61}$$

$$= \sum_h \alpha(y=x_d,h)\;\frac{2sh^2}{\sqrt{s^2z_d^2+s^2h^2}}\;\frac{sz_d}{\sqrt{s^2z_d^2+s^2h^2}} \tag{3.62}$$

$$= \sum_h \alpha(y=x_d,h)\;\frac{2h^2z_d}{z_d^2+h^2} \tag{3.63}$$

$$\approx \frac{1}{\Delta h}\int_0^{L/2} dh\;\;\alpha(y=x_d,h)\;\frac{2h^2z_d}{z_d^2+h^2} \tag{3.64}$$

$$\approx \frac{4z_d\,N_h}{L}\int_0^{L/2} dh\;\;\alpha(y=x_d,h)\;\frac{h^2}{z_d^2+h^2} \tag{3.65}$$

where L is the recording cable length, and N_h is the number of offsets used; I assume for simplicity that the innermost offset is small enough to be taken as zero.

The evaluation of this integral is particularly simple if one takes $\alpha_{\theta=0}(y=x_d, h) = z_d^2 + h^2$. This choice of weight is not completely coincidental; in Appendix D, I show that this is exactly the weighting needed to convert the linearized least squares solution I have used here into the x^2–t^2 parametrization that Toldi used. Using this substitution one gets

$$\mathbf{t_s}\cdot\mathbf{t_r} \approx \frac{4 z_d N_h}{L} \int_0^{L/2} dh \quad h^2 \tag{3.66}$$

$$\approx \frac{N_h L^2 z_d}{6} . \tag{3.67}$$

Similarly one gets

$$\mathbf{t_s}\cdot\mathbf{t_s} \approx \frac{8 N_h}{L} \int_0^{L/2} dh \;\; h^4 \tag{3.68}$$

$$\approx \frac{N_h L^4}{20} \tag{3.69}$$

and

$$\mathbf{t_r}\cdot\mathbf{t_r} \approx \frac{2 N_h z_d^2}{L} \int_0^{L/2} dh \tag{3.70}$$

$$\approx N_h z_d^2 \tag{3.71}$$

and then

$$D \approx \frac{N_h^2 L^4 z_d^2}{45} . \tag{3.72}$$

One also has

$$t_s(y_\theta, h_\theta) = \frac{2\gamma^2 (x_a - x_d)^2}{\sqrt{z_d^2 + \gamma^2 (x_a - x_d)^2}} \tag{3.73}$$

and

$$t_r(y_\theta, h_\theta) = \frac{z_d}{\sqrt{z_d^2 + \gamma^2 (x_a - x_d)^2}} . \tag{3.74}$$

Plugging in these terms into equations (3.58) and (3.59) yields

$$A_s(y_\theta,h_\theta) = \frac{z_d^2 N_h\,[12\gamma^2(x_a-x_d)^2-L^2]}{6\sqrt{z_d^2+\gamma^2(x_a-x_d)^2}} \tag{3.75}$$

and

$$A_\tau(y_\theta,h_\theta) = \frac{z_d\,N_h\,L^2[3L^2-20\gamma^2(x_a-x_d)^2]}{60\sqrt{z_d^2+\gamma^2(x_a-x_d)^2}}\ . \tag{3.76}$$

If these are substituted into equation (3.37) with $\alpha(y_\theta,h_\theta)=z_d^2+\gamma^2(x_a-x_d)^2$ the result is that

$$(G_s)_{\theta=0}(\mathbf{d},\mathbf{a}) = \frac{2N_h\,\gamma}{z_d\,DL}\left[z_d^2+\gamma^2(x_a-x_d)^2\right]^{3/2} A\left[y_\theta(\mathbf{d},\mathbf{a}),h_\theta(\mathbf{d},\mathbf{a})\right] \tag{3.77}$$

$$= \frac{15\gamma}{z_d\,L^5}\left[z_d^2+\gamma^2(x_a-x_d)^2\right]\left[12\gamma^2(x_a-x_d)^2-L^2\right]. \tag{3.78}$$

Letting $L'=L/\gamma$ and shuffling terms around yields

$$(G_s)_{\theta=0}(\mathbf{d},\mathbf{a}) = \frac{15z_d}{L^2L'}\left[3\left(\frac{2(x_a-x_d)}{L'}\right)^2-1\right]\left[1+\frac{L^2}{4z_d^2}\left(\frac{2(x_a-x_d)}{L'}\right)^2\right] \tag{3.79}$$

which is just equation (4.18) of p.77 of Toldi (1985) with minor notational changes.

The similar expression for G_τ becomes

$$(G_\tau)_{\theta=0}(\mathbf{d},\mathbf{a}) = \frac{2N_h\,\gamma}{z_d\,DL}\left[z_d^2+\gamma^2(x_a-x_d)^2\right]^{3/2} B\left[y_\theta(\mathbf{d},\mathbf{a}),h_\theta(\mathbf{d},\mathbf{a})\right] \tag{3.80}$$

$$= \frac{3\gamma}{2z_d^2L^3}\left[z_d^2+\gamma^2(x_a-x_d)^2\right]\left[3L^2-20\gamma^2(x_a-x_d)^2\right] \tag{3.81}$$

$$= \frac{3}{2L'}\left[3-5\left(\frac{2(x_a-x_d)}{L'}\right)^2\right]\left[1+\frac{L^2}{4z_d^2}\left(\frac{2(x_a-x_d)}{L'}\right)^2\right]. \tag{3.82}$$

Toldi did not present this result, but following through the same line of analysis he used to derive G_s yields exactly equation (3.82). I note that for $L \ll z$ this almost reduces to Loinger's (1983) result, but has a leading factor of $3/2L'$ where he had $3/4$. I believe that this result is correct and that Loinger's equation has a minor error.

For zero dip, the choice of a particular weighting function made it possible to approximate all the inner product sums by simple integrals and to re-derive the simple, closed form algebraic expressions found by Toldi. However, for non-zero dip,

closed form solutions become much too complicated to provide any hope of gaining insight from their form, and I do not derive them here.

3.9 VISUALIZING THE OPERATOR

The operators $\mathbf{G}_s$, $\mathbf{G}_r$, and $\mathbf{G}_y$ are functions of the four variables x_a, z_a, x_d, and z_d describing the locations of an anomaly **a** and a reflecting point **d**. Four dimensional pictures are difficult to comprehend. It is easiest to look at the operators either for a fixed anomaly **a** or for a fixed reflecting point **d**. The latter is the form in which the operator is most easily applied, so I consider it first. For simplicity, I compute the operators against a background with constant slowness of 0.5 s/km, which is physically of the right magnitude for rocks and conveniently cancels out scaling factors of $2s$. Note that kilometers and seconds are good units to use here, because distances, times and slownesses will ordinarily then all be of the same magnitude. This is important because the inversion uses parameters with different physical dimensions (slownesses, times, and distances), and the condition number of **A** can be adversely affected by poor scaling of units. I discuss scaling of units further in section 4.5.

Flat bed operators

Figure 3.6 shows the operator $\mathbf{G}_s$ for a single fixed reflecting point **d** and dip angle θ=0. The point **d** is located at the apex of the triangular region in the upper picture; one can think of this as isolating for examination one point on a flat bed through this location. The picture then displays the magnitude of change in the migration slowness measured at the point **d** caused by a perturbation in the interval slowness anywhere else. The gray background indicates no change; because of the finite cable aperture, slowness anomalies outside the central triangular region cannot affect the migration slowness at the point **d**. Within the triangular region, light areas indicate positive changes and dark areas negative changes. To clarify this pattern, the lower picture in Figure 3.6 shows a cross-section along the top of the upper picture. Here, amplitude of $\mathbf{G}_s$ is plotted as a function of x_a with z_a held constant.

The origin of the pattern of positive response for wide offset rays and negative response for inner offsets is illustrated schematically in Figure 3.7. A negative interval slowness anomaly causes an anomalously fast traveltime one offset. This traveltime anomaly can cause either a positive or a negative change in the slowness that describes the best fitting hyperbola. If it is at inner offset, it pulls up the peak of the hyperbola and yields a greater slowness, but if it is at outer offsets, it pulls up the

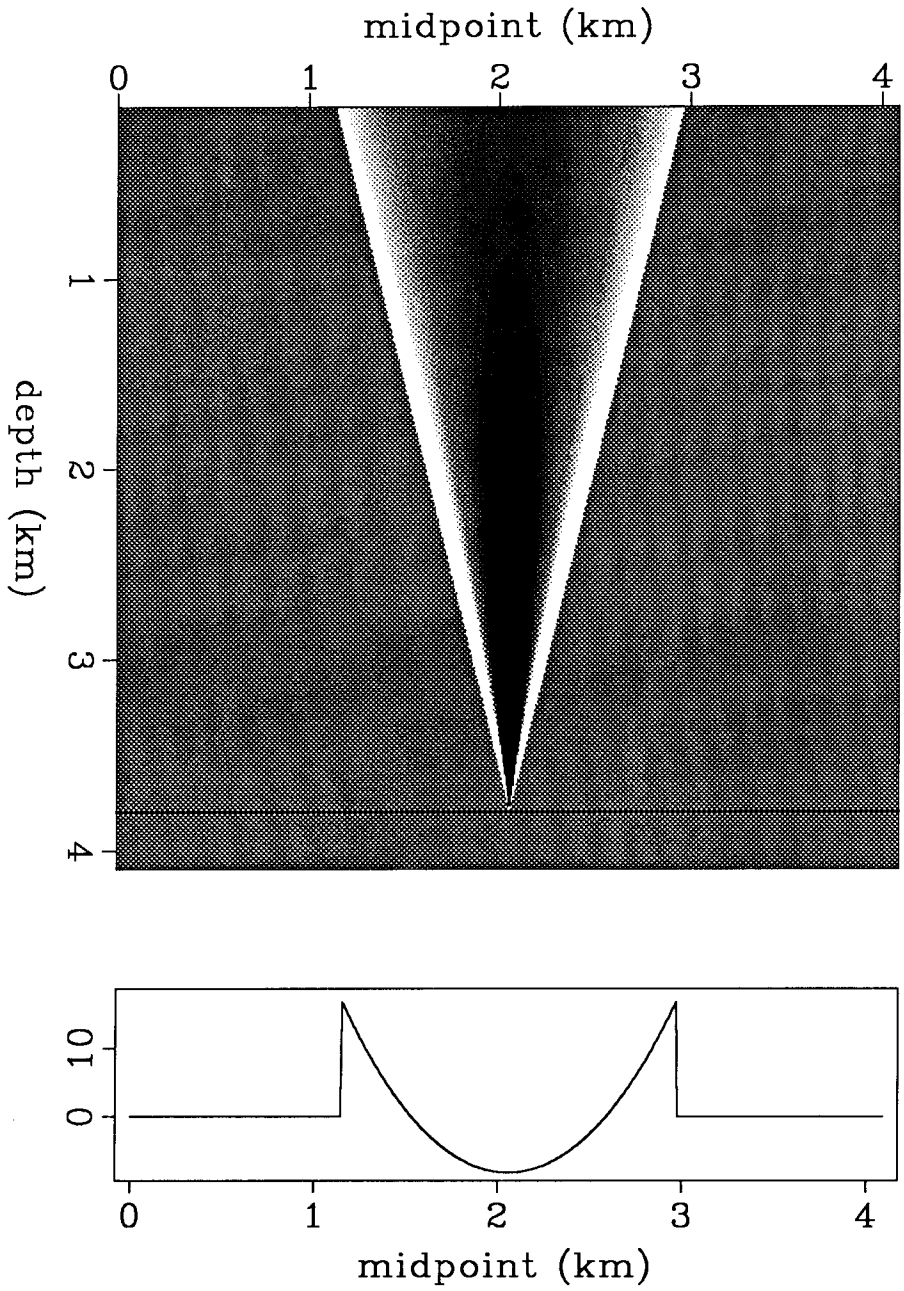

FIG. 3.6. The operator $\mathbf{G}_s$ for a single fixed reflecting point $\mathbf{d}$ and dip angle θ=0. The upper picture displays the magnitude of change in the migration slowness s_d measured at a point $\mathbf{d}$, caused by a perturbation in the interval slowness at any other point. The point $\mathbf{d}$ is located at the apex of the triangular region. The gray background indicates no change, light areas indicate positive response, and dark areas indicate negative response. The lower picture graphs amplitude of $\mathbf{G}_s$ for a flat bed, plotted as a function of lateral anomaly position x_a with anomaly depth z_a held constant. This picture corresponds to a cross-section along the top of the upper picture. Wide offsets show a positive response, and inner offsets a negative response.

tails, so the slowness of the best fitting hyperbola is less. The effect on the zero-offset intercept time τ is just the opposite.

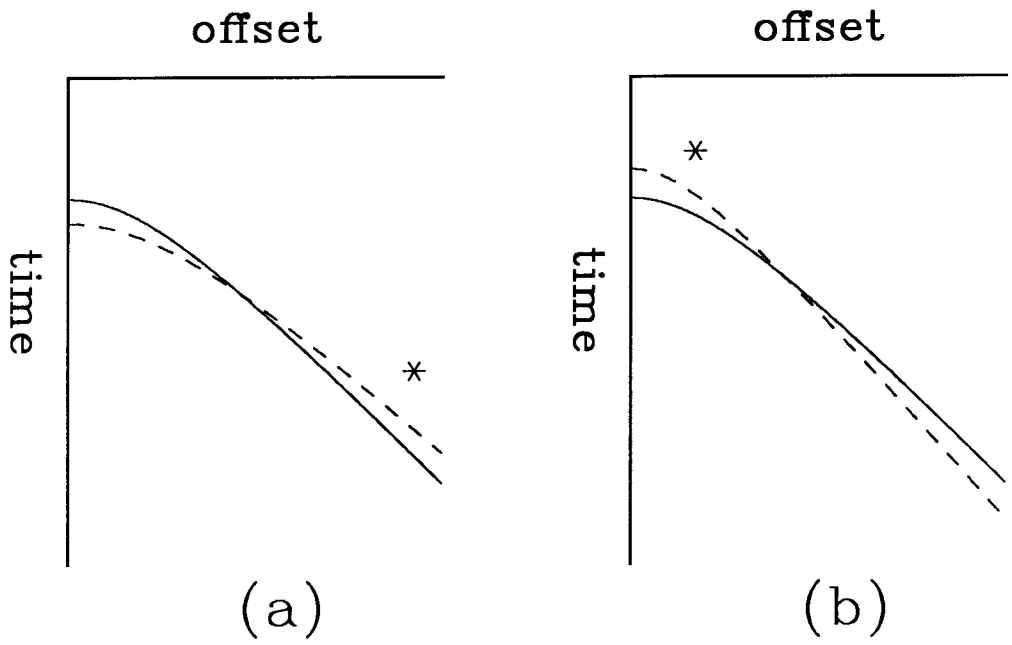

FIG. 3.7. An anomalously fast traveltime can cause the stacking slowness either to increase or decrease. The solid line in each figure shows an unperturbed moveout hyperbola. The anomalous traveltime is represented by the asterisk. The dashed line represents the perturbed moveout hyperbola, incorporating the anomalous traveltime. If the anomaly is at outer offsets (left picture), the stacking slowness decreases. If the anomaly is at inner offsets (right picture), the stacking slowness increases.

Figure 3.8 shows the operator $\mathbf{G}_\tau$ for θ=0. The pattern is similar to that of $\mathbf{G}_s$ in Figure 3.6 but this time with negative changes at wide offsets and positive changes at inner offsets. The lower picture in Figure 3.8 again shows a cross-section along the top of the upper picture, graphing the magnitude of $\mathbf{G}_\tau$ for fixed z_a and varying x_a. No figure is shown for $\mathbf{G}_y$, because, as discussed above, it is identically zero for flat beds.

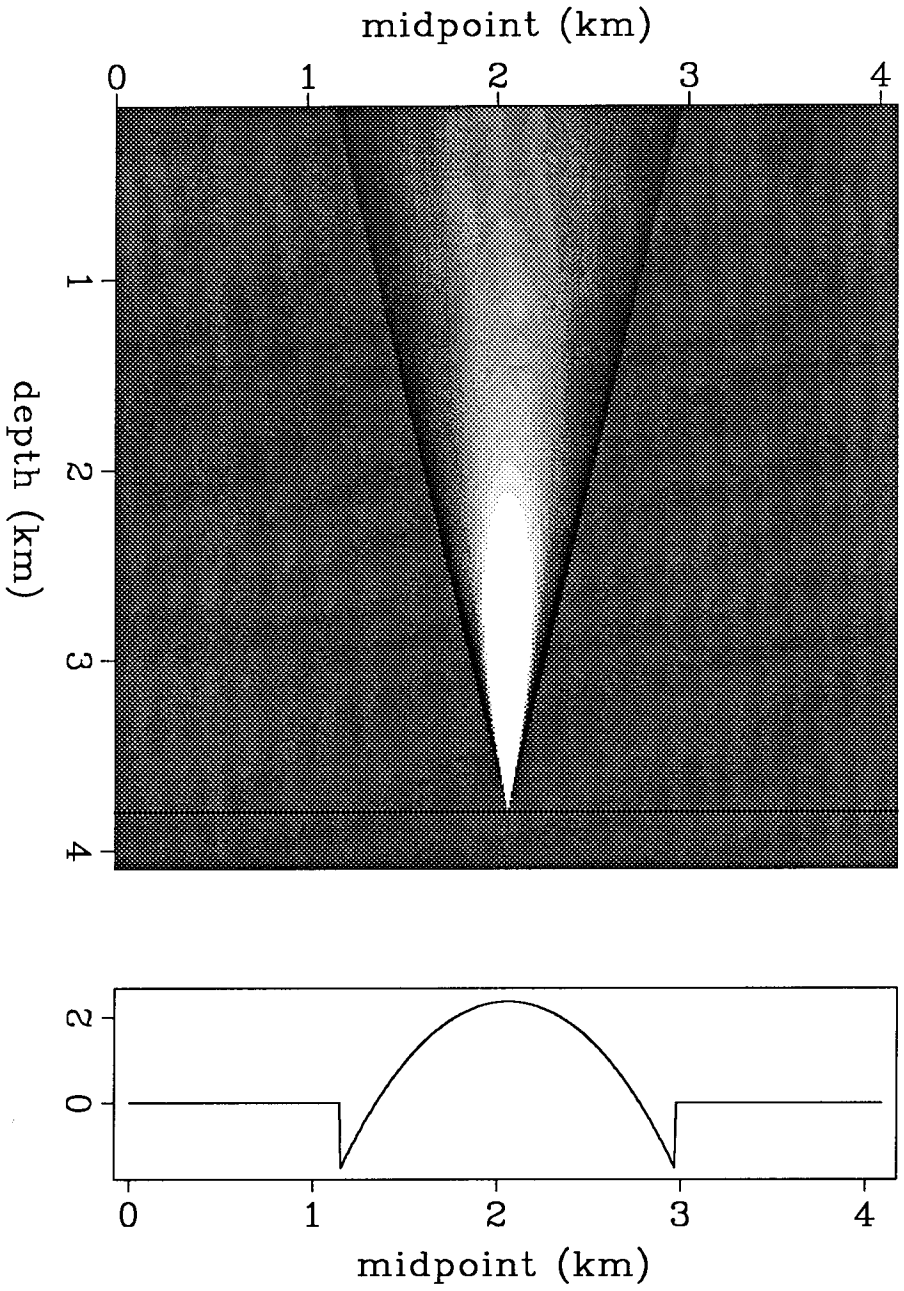

FIG. 3.8. The operator $\mathbf{G}_\tau$ for a single fixed reflecting point $\mathbf{d}$ and dip angle θ=0. The upper picture displays the magnitude of change in the migrated time location τ_d of a point $\mathbf{d}$, caused by a perturbation in the interval slowness at any other point. The point $\mathbf{d}$ is located at the apex of the triangular region. The gray background indicates no change, light areas indicate positive response, and dark areas indicate negative response. The lower picture graphs amplitude of $\mathbf{G}_\tau$ for a flat bed, plotted as a function of lateral anomaly position x_a with anomaly depth z_a held constant. This picture corresponds to a cross-section along the top of the upper picture. Wide offsets show a negative response, and inner offsets a positive response, the opposite of the pattern for $\mathbf{G}_s$ in Figure 3.6.

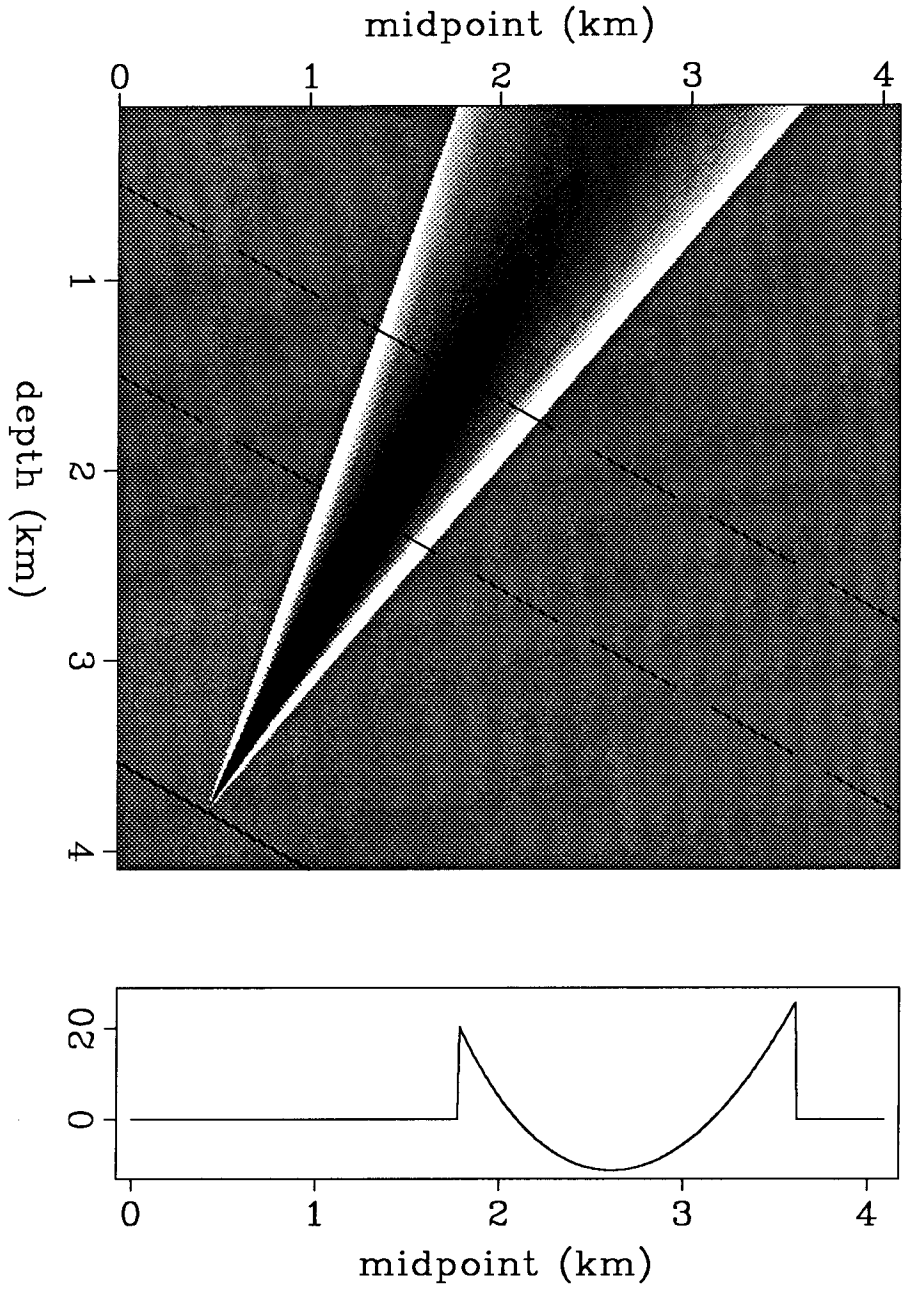

FIG. 3.9. The operator $\mathbf{G}_s$ for a single fixed reflecting point $\mathbf{d}$ and dip angle θ=30. The upper picture displays the magnitude of change in the migration slowness s measured at a point $\mathbf{d}$, caused by a perturbation in the interval slowness at any other point. The point $\mathbf{d}$ is located at the apex of the triangular region. The gray background indicates no change, light areas indicate positive response, and dark areas indicate negative response. The operator is similar to the flat dip operator in Figure 3.6, but skewed by the dip. The lower picture graphs amplitude of $\mathbf{G}_s$ for a dipping bed, plotted as a function of lateral anomaly position x_a with anomaly depth z_a held constant. This picture corresponds to a cross-section along the top of the upper picture. The dashed lines in the upper picture correspond to the cross-sections in Figure 3.10.

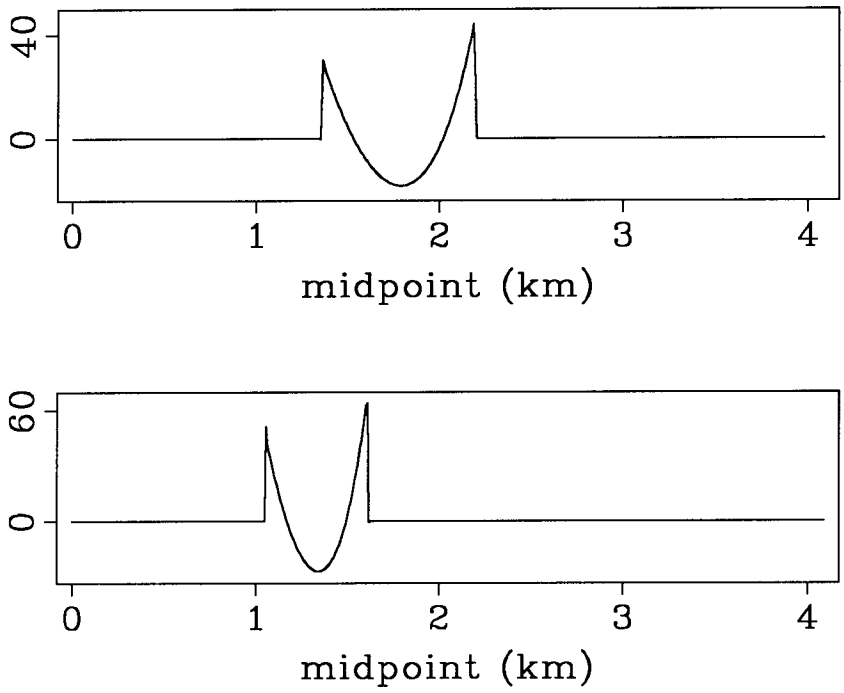

FIG. 3.10. Cross sections through the $\mathbf{G}_s$ operator of Figure 3.9. These cross-sections are along the dashed lines in figure 3.9, parallel to the dipping reflector.

Dipping bed operators

The ray picture in Figure 3.3 for a common-reflection point gather and non-zero dip θ is similar to that for flat beds, but skewed by the dip. Likewise, the operator $\mathbf{G}_s$ for non-zero θ is similar to the flat bed of Figure 3.6, but again skewed. This operator $\mathbf{G}_s$ for a 30 degree dip is shown in Figure 3.9. The pattern of positive response at wide offsets and negative at inner offsets is again seen. Note that the minimum of the response pattern is now not at the middle of the aperture, but instead at the location of the normal ray.

I have emphasized that the dipping bed operator is *similar* to a skewed version of the flat bed operator. However, it is not *identical.* The flat bed operator is symmetric around the vertical ray; the dipping bed operator is *not* exactly symmetric around the normal ray. Figure 3.10 shows two cross-sections through the operator of Figure 3.9, this time taken parallel to the dipping reflector rather than parallel to the surface. The peak amplitudes at the outermost offsets are not exactly equal, as they are for the flat bed operator cut horizontally. The amplitude of $\mathbf{G}_s$ depends on the reflector depth, the anomaly depth, the dip angle, and the shooting geometry. These

factors balance each other only for the flat-bed operator. In particular, the two cosine factors in equation (3.12) that compensate for the conversion from integration over arc length along a ray to integration over depth are equal only for the flat dip operator.

Figure 3.11 shows the operator $\mathbf{G}_\tau$ for θ=30. Again, comparison with the flat bed operator in Figure 3.8 shows that the dipping-bed migration slowness operator is similar to the flat-bed stacking slowness operator, but skewed by the dip angle.

Figure 3.12 shows the operator $\mathbf{G}_y$. Because the dip is not zero, this operator is no longer identically zero. As suggested by equation (3.45), $\mathbf{G}_y$ is proportional to $\mathbf{G}_\tau$.

So far I have shown the operator for a fixed reflecting point. The conjugate operator predicts the effect at all data points of a single anomaly point. Figure 3.13 shows an example of this conjugate $\mathbf{G}_s$ operator for flat beds, and Figure 3.14 shows a series of cross-sections through this operator. These cross-sections can be compared with similar graphs in Figure 4.6 of Toldi (1985) or Figure 2 of Loinger (1983). For flat beds (θ=0), prestack time migration is essentially just NMO stacking, and this operator should be the same as those used by Toldi (1985) or Loinger (1983). As I showed in section 3.8, the migration operator I use here does indeed formally reduce to Toldi's stacking slowness operator for flat beds, and numerical testing confirms that the different choice of weighting functions causes only minor discrepancies.

From the analytic solution for the flat dip operator, equation 3.79, one can easily show that the amplitude of the $\mathbf{G}_s$ operator is proportional to $z_d^2/(z_d - z_a)$. This effect can be seen in Figure 3.13. The amplitude increases with depth z_d, except near the anomaly where the denominator term takes over to generate a singularity as **d** approaches **a**. Similarly, Figure 3.15 shows the conjugate $\mathbf{G}_s$ operator for a single anomaly point and 30 degree dip, and Figure 3.16 shows cross-sections. Note that the leg of the operator with peak amplitude can be skewed either updip or downdip.

Wide offset operator

All of the pictures of operators presented so far have assumed that the innermost offset is zero. Nothing in the theory requires this to be true. In practice, stacks over various offset ranges are sometimes compared for velocity analysis. Figure 3.17 shows the operator $\mathbf{G}_s$ for an experiment in which only the outer offsets are used. Note that the pattern of positive and negative responses is still seen, but that

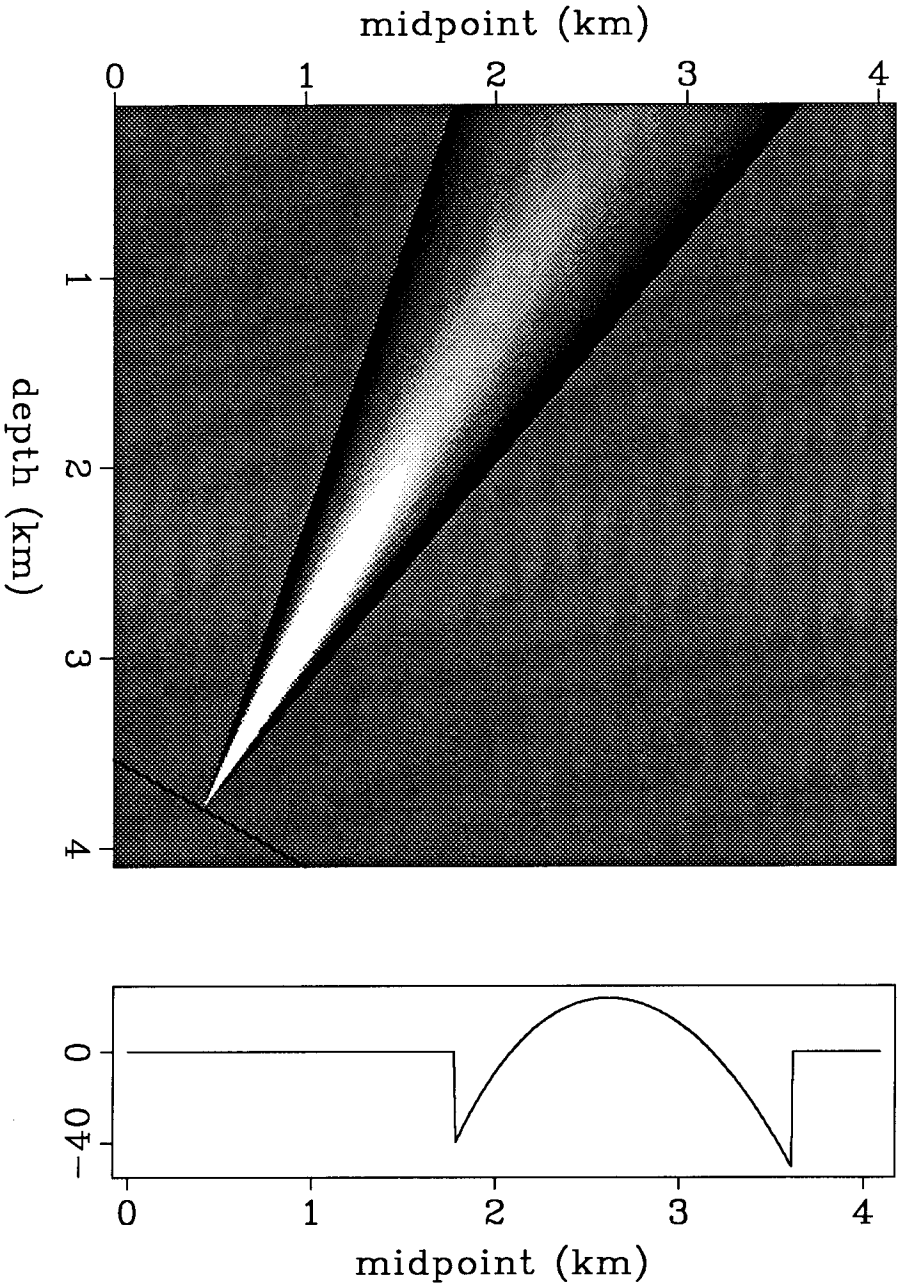

FIG. 3.11. The operator $\mathbf{G}_\tau$ for a single fixed reflecting point **d** and dip angle θ=30. The upper picture displays the magnitude of change in the migrated time location τ_d of a point **d**, caused by a perturbation in the interval slowness at any other point. The point **d** is located at the apex of the triangular region. The gray background indicates no change, light areas indicate positive response, and dark areas indicate negative response. The operator is similar to the flat dip operator in Figure 3.8, but skewed by the dip. The lower picture graphs amplitude of $\mathbf{G}_\tau$ for a dipping bed, plotted as a function of lateral anomaly position x_a with anomaly depth z_a held constant. in Figure 3.8. This picture corresponds to a cross-section along the top of the upper picture.

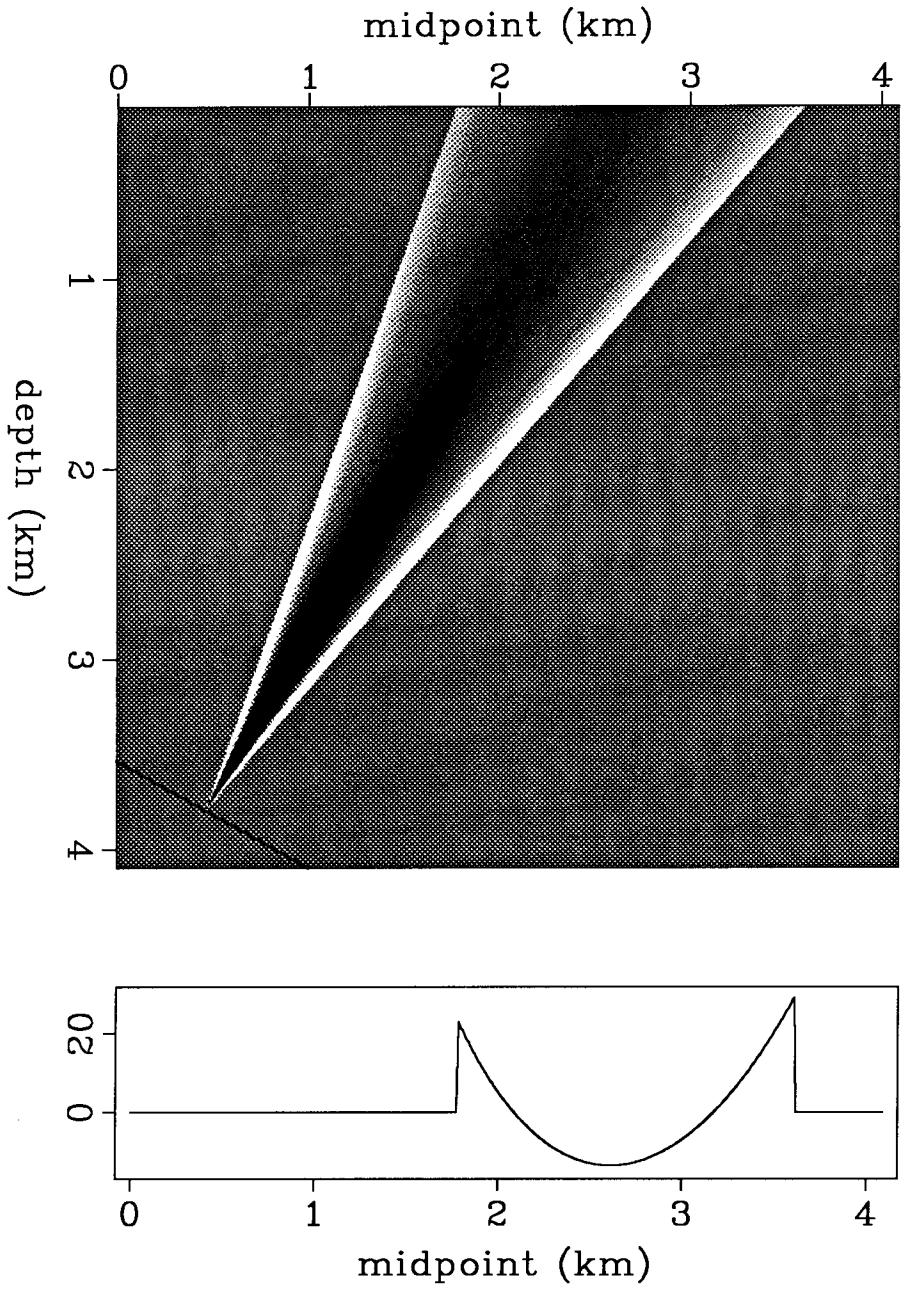

FIG. 3.12. The operator $\mathbf{G}_y$ for a single fixed reflecting point $\mathbf{d}$ and dip angle θ=30. The upper picture displays the magnitude of change in the migrated location y_d of a point $\mathbf{d}$, caused by a perturbation in the interval slowness at any other point. The point $\mathbf{d}$ is located at the apex of the triangular region. The gray background indicates no change, light areas indicate positive response, and dark areas indicate negative response. The lower picture graphs amplitude of $\mathbf{G}_y$ for a dipping bed, plotted as a function of lateral anomaly position x_a with anomaly depth z_a held constant. This picture corresponds to a cross-section along the top of the upper picture. The pattern is proportional to that for $\mathbf{G}_\tau$ in Figure 3.10 but opposite in sign.

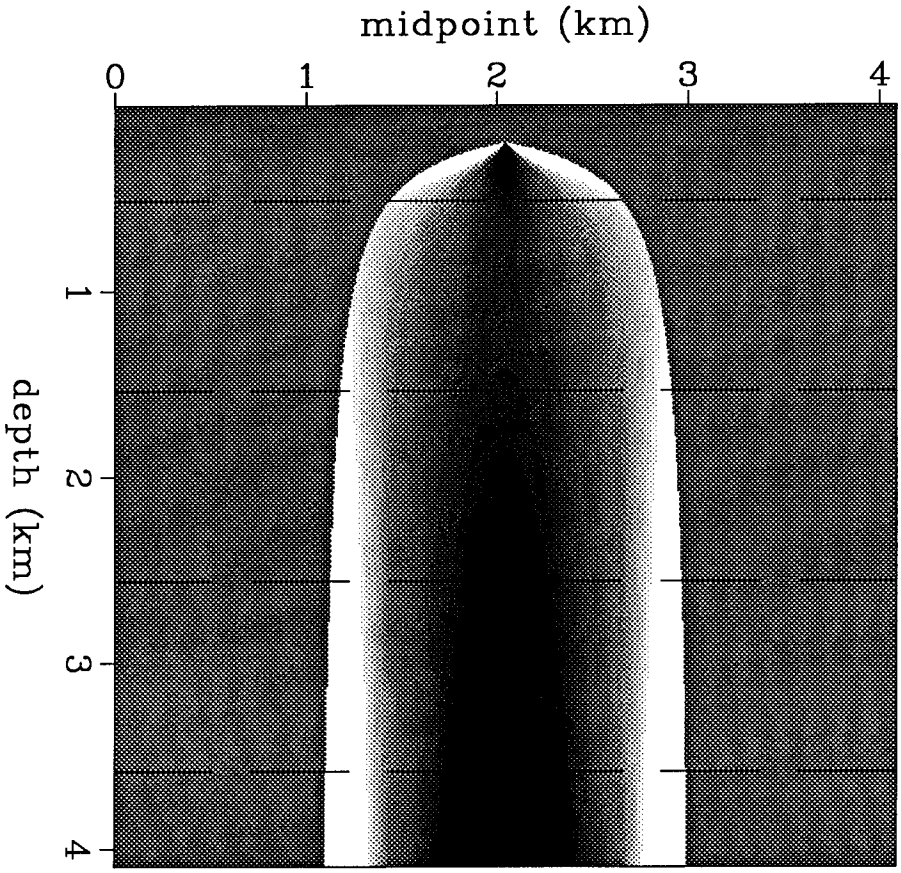

FIG. 3.13. The operator $\mathbf{G}_s$ for a single fixed anomaly point **a** and dip angle θ=0. This picture displays the magnitude of change in the migration slowness s caused by a perturbation in the interval slowness at a point **a**, as measured at any other point. The point **a** is located at the apex of the triangular region. The gray background indicates no change, light areas indicate positive response, and dark areas indicate negative response. The dashed lines correspond to the cross-sections in Figure 3.14.

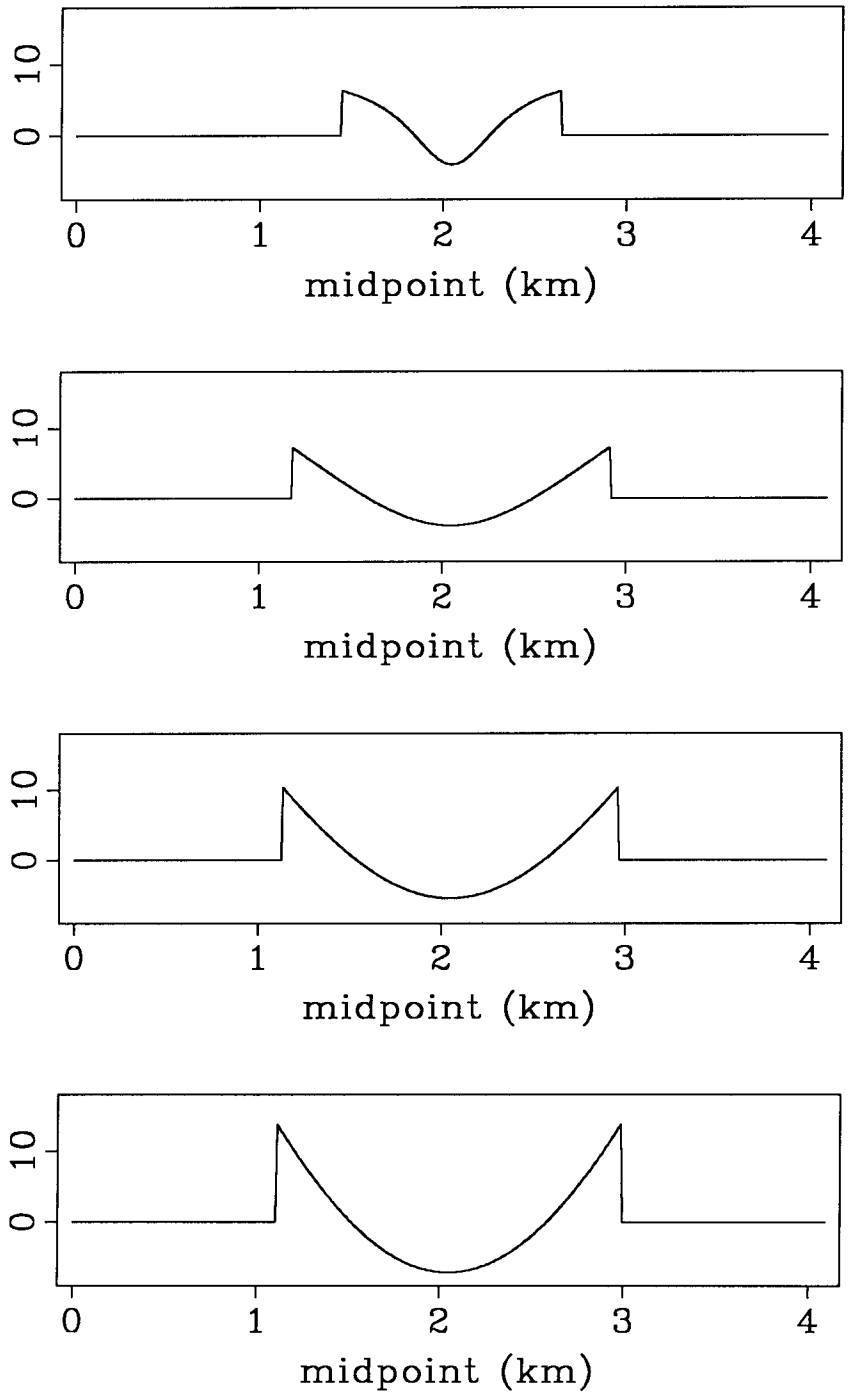

FIG. 3.14. The operator $\mathbf{G}_s$ for a single fixed anomaly point $\mathbf{a}$ and dip angle θ=0. This picture displays the magnitude of change in the migration slowness s caused by a perturbation in the interval slowness at a point $\mathbf{a}$, as measured along flat beds at various depths. These plots correspond to cross-sections along the dashed lines in Figure 3.13.

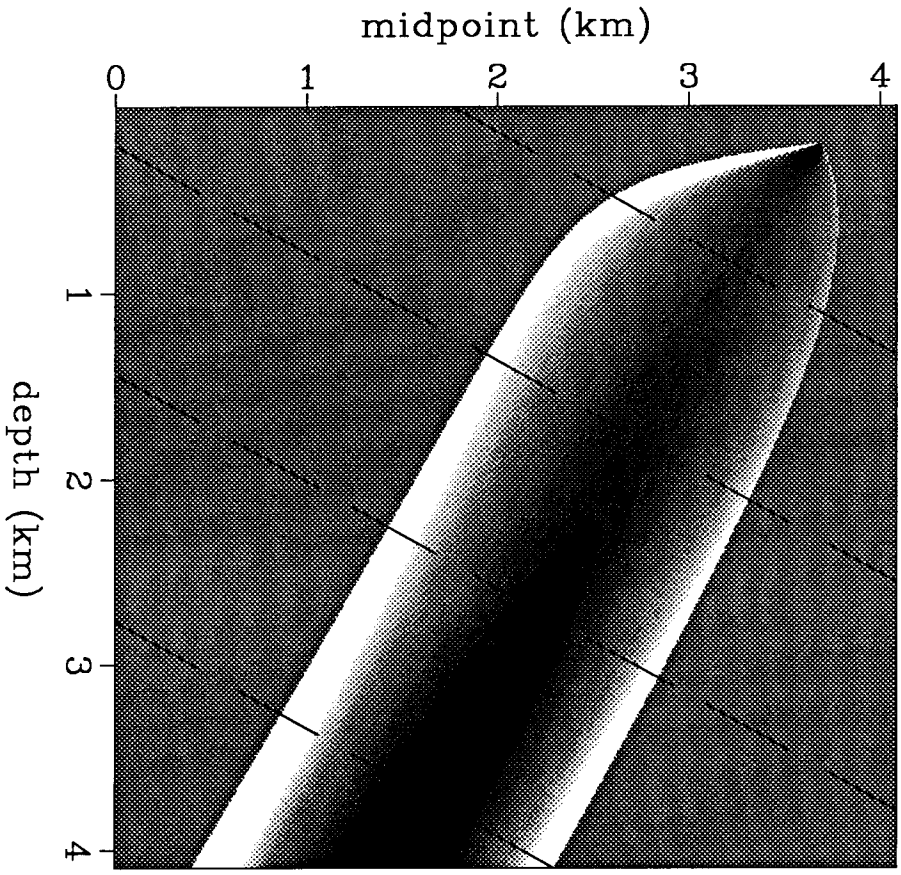

FIG. 3.15. The operator $\mathbf{G}_s$ for a single fixed anomaly point **a** and dip angle θ=30. This picture displays the magnitude of change in the migration slowness s caused by a perturbation in the interval slowness at a point **a**, as measured at any other point. The point **a** is located at the apex of the triangular region. The gray background indicates no change, light areas indicate positive response, and dark areas indicate negative response. The dashed lines correspond to the cross-sections in Figure 3.16.

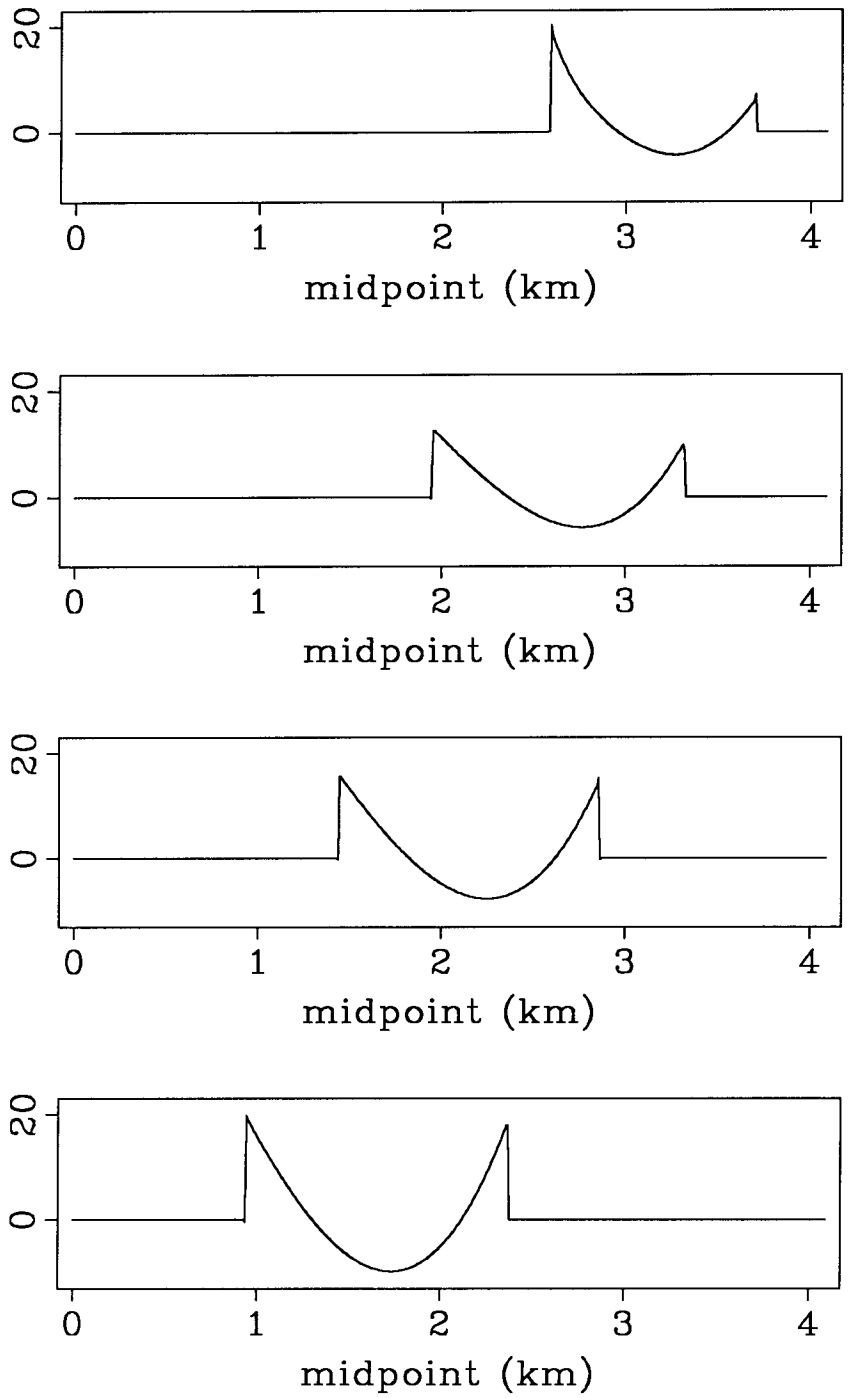

FIG. 3.16. The operator $\mathbf{G}_s$ for a single fixed anomaly point $\mathbf{a}$ and dip angle θ=30. This picture displays the magnitude of change in the migration slowness s caused by a perturbation in the interval slowness at a point $\mathbf{a}$, as measured along dipping beds at various depths. These plots correspond to cross-sections along the dashed lines in Figure 3.15. Note that both the amplitudes and the skew change with depth of the reflector.

this operator is *not* just the zero-inner offset operator with the middle section discarded. I use this operator further in section 4.4.

Variable slowness background

For simplicity, the illustrations of operators so far have assumed that they are computed against a constant slowness background. This is not required by the theory, and for an iterative nonlinear inversion one would want to update the background slowness model repeatedly. The behavior of the operator remains similar, but its computation requires tracing rays, and the shape of the operator follows the curvature of these rays. Figure 3.18 shows an example of the $\mathbf{G}_s$ operator computed for 30 degree dip and a depth-variable background slowness. Because the rays turn upward, the effective dip is less at shallow depths, and the operator is closer to symmetric.

DMO operators

In chapter 2 I showed how prestack time-migration slownesses could be derived from stacking slownesses using DMO-corrected slownesses as an intermediate step. The migration slowness operator $\mathbf{G}_s$ discussed in this chapter can also be used to predict the DMO slownesses. DMO slownesses are, in fact, the same as migration slownesses; the difference lies not in the $\mathbf{G}_s$ operator, but in the affiliated mapping between the subsurface reflecting point (x_d, z_d) and the location (y_d, τ_d) in the data where it appears. Prestack time migration can be decomposed into the sequence of NMO, DMO, stack, and post-stack time migration. The difference between DMO slowness analysis and prestack time migration slowness analysis is thus just the repositioning of events caused by the post-stack migration. In terms of the generalized summation curves shown in Figure 3.4, both methods sum data over the same paths; the DMO analysis assigns the result to the zero-offset intercept of the curve (the unmigrated position), while the migration analysis assigns the result to the apex of the pyramid (the migrated location). That is, if (y, τ) is the migrated position (the apex of the pyramid), the unmigrated position (y_{dmo}, t_{dmo}) is given by

$$y_{dmo} = y - \frac{\tau}{2s} \tan\theta \tag{3.83}$$

and

$$t_{dmo} = \tau \sec\theta \ . \tag{3.84}$$

Note that these equations relate two positions on the fitting pyramid, which is

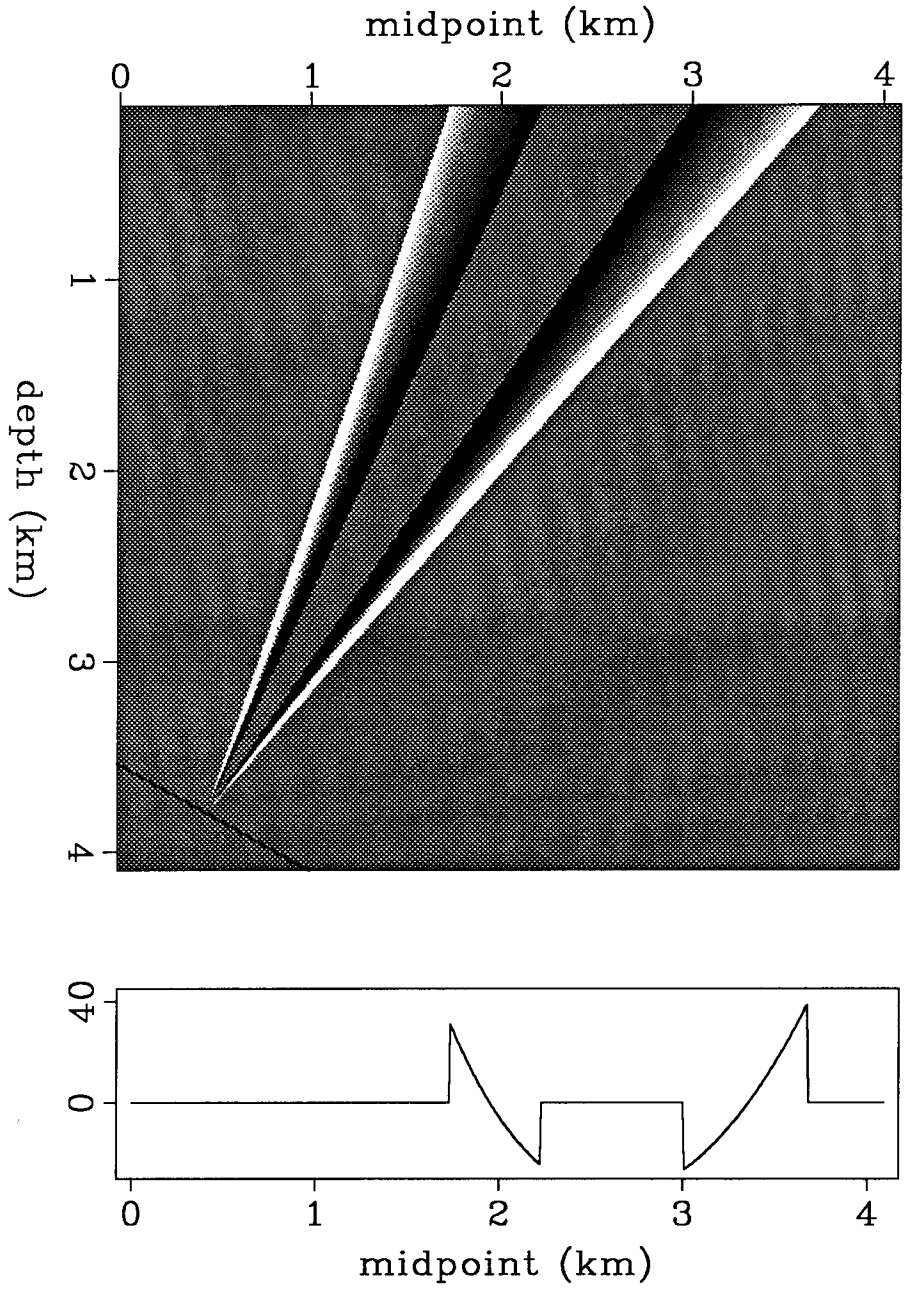

FIG. 3.17. The operator $\mathbf{G}_s$ for a single fixed reflecting point $\mathbf{d}$ and dip angle θ=30, with non-zero innermost offset. The upper picture displays the magnitude of change in the migration slowness s measured at a point $\mathbf{d}$, caused by a perturbation in the interval slowness at any other point. The point $\mathbf{d}$ is located at the apex of the triangular region. The gray background indicates no change, light areas indicate positive response, and dark areas indicate negative response. The operator is similar to the full-cable operator in Figure 3.9, but is not just that operator with the central section removed; both positive and negative responses will always be seen . The lower picture graphs amplitude of $\mathbf{G}_s$ for the operator in the upper picture, plotted as a function of lateral anomaly position x_a with anomaly depth z_a held constant. This picture corresponds to a cross-section along the top of the upper picture.

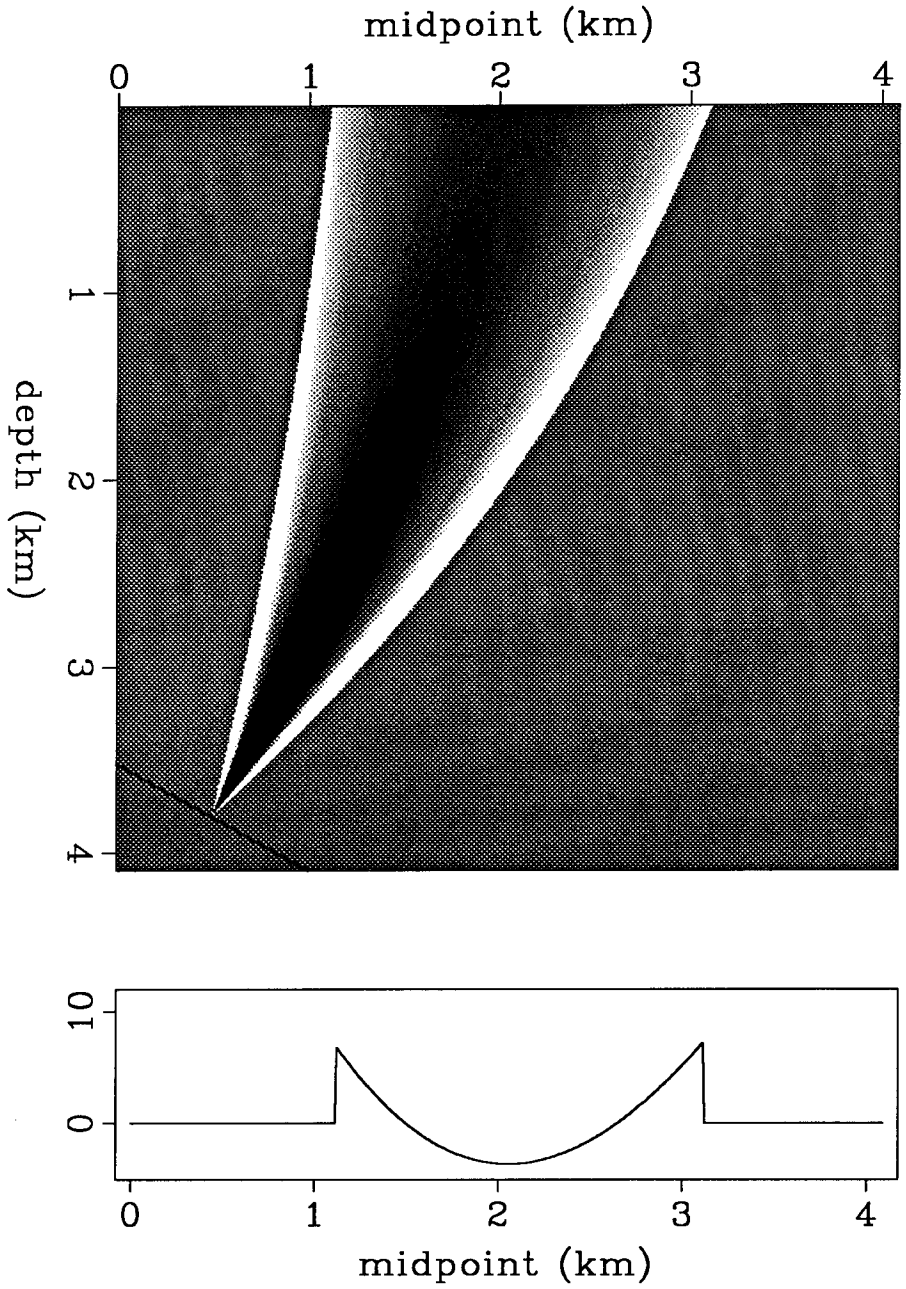

FIG. 3.18. The operator $\mathbf{G}_s$ for a single fixed reflecting point $\mathbf{d}$ and dip angle θ=30, with a depth-variable background slowness. The upper picture displays the magnitude of change in the migration slowness s measured at a point $\mathbf{d}$, caused by a perturbation in the interval slowness at any other point. The point $\mathbf{d}$ is located at the apex of the triangular region. The gray background indicates no change, light areas indicate positive response, and dark areas indicate negative response. The operator is similar to the constant slowness operator in Figure 3.9, but curved because of ray bending. The lower picture graphs amplitude of $\mathbf{G}_s$ for a dipping bed, plotted as a function of lateral anomaly position x_a with anomaly depth z_a held constant. This picture corresponds to a cross-section along the top of the upper picture.

always constant-slowness, and do not necessarily describe the relation between the true migrated and unmigrated positions. If the slowness analysis algorithm attempts to maximize the energy in the resulting image, only the summation over offset h contributes; the repositioning caused by the zero-offset migration focuses the image, but does not change the total energy in the image as a whole.

Against a constant slowness background, the mapping from model position to data position for the migration slowness analysis is just a relabeling of the vertical axis: $(y_d, \tau_d) = (x_d, 2sz_d)$. The mapping for the DMO slowness analysis must undo the zero-offset migration, and so is dip-dependent: $(y_d, t_d) = (x_d - z_d \tan\theta,\ 2sz_d \sec\theta)$. Note that for the DMO analysis, I use t to indicate unmigrated time instead of τ which I have used previously for migrated time. For a variable slowness background, the map from physical subsurface reflector location to data position requires ray tracing. For the migrated data, the map requires tracing *image* rays; for the unmigrated DMO analysis, it is *normal* rays that are needed (Hubral, 1977).

In Figure 3.19 I show the expected DMO slowness changes caused by a perturbation in the interval slowness at one point, as seen on 30 degree dipping beds. All locations are now given not in terms of x and z, but as the corresponding values of y and t. This picture is a stretched version of 3.15; the underlying operator $\mathbf{G}_s$ is the same, because the same family of rays (common reflection point gathers) is being used. Figure 3.20 shows cross-sections through the DMO operator of Figure 3.19. The cross-sections are taken with an apparent angle less than the true dip angle of 30 degrees, because the vertical axis of Figure 3.19 is unmigrated time instead of depth.

3.11 CONCLUSIONS

Perturbations in interval slownesses can be related to the changes that they cause in measurable migration slownesses by a linear operator. This operator can be formulated as a filtered version of conventional tomographic back-projection. It can be implemented stably using singular value decomposition to solve for the filtering stage by inverting double-square-root traveltime equations. For flat beds this operator reduces both theoretically and numerically to Toldi's stacking slowness operator. For dipping beds, the operator still resembles the flat bed one, but is skewed by the effect of the dip. The same operator can also be used to relate changes in interval slowness to changes in DMO-corrected stacking slowness; the only difference is that velocities are assigned to unmigrated, rather than migrated, positions.

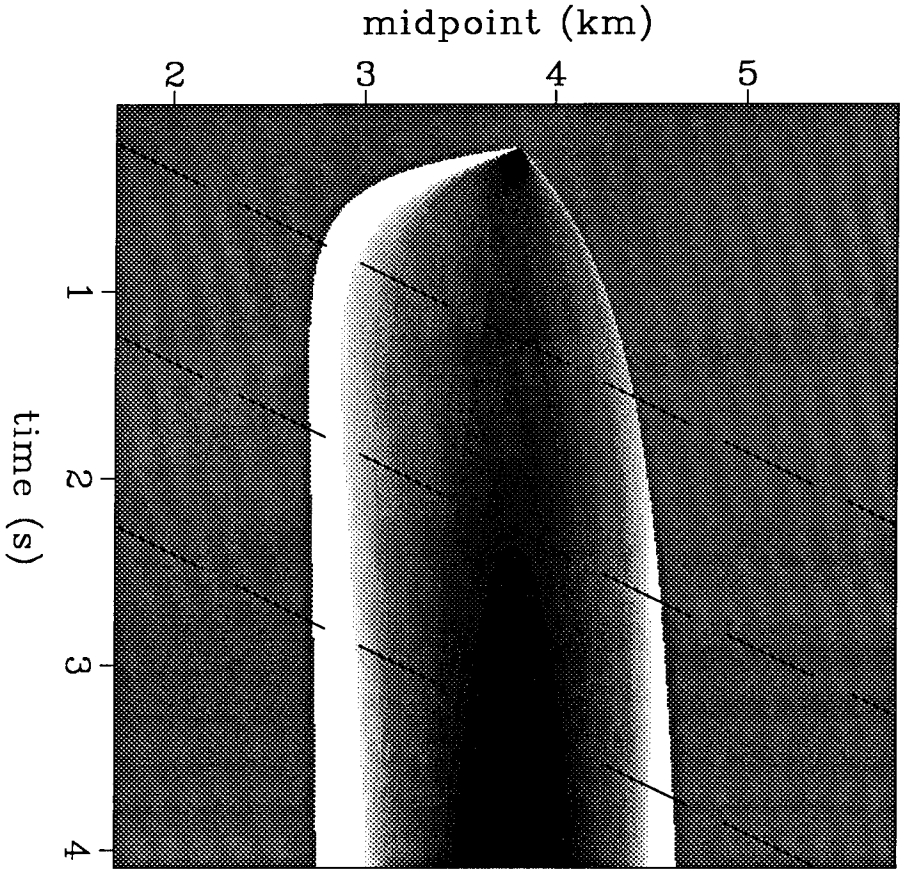

FIG. 3.19. The DMO slowness operator for a single fixed anomaly point **a** and dip angle θ=30. This picture displays the magnitude of change in the DMO slowness s caused by a perturbation in the interval slowness at a point **a**, as measured at any other point. The point **a** is located at the apex of the triangular region. The gray background indicates no change, light areas indicate positive response, and dark areas indicate negative response. The dashed lines correspond to the cross-sections in Figure 3.20.

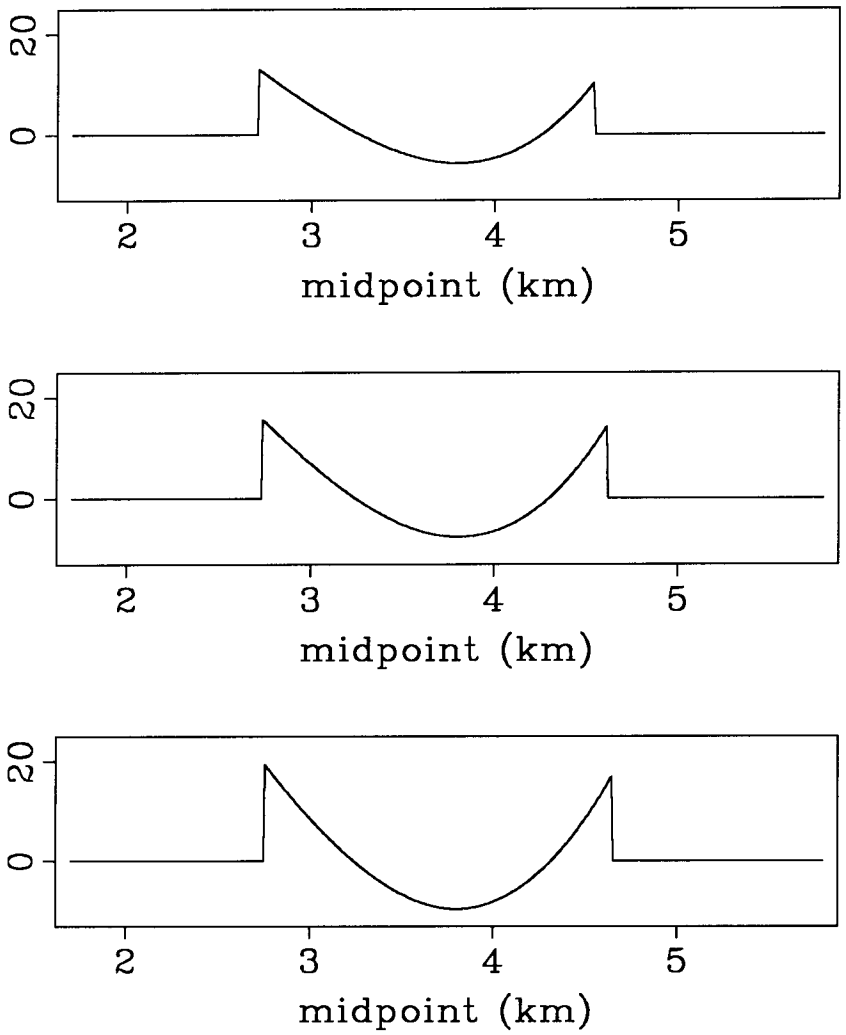

FIG. 3.20. The DMO slowness operator for a single fixed anomaly point **a** and dip angle θ=30. This picture displays the magnitude of change in the DMO slowness s caused by a perturbation in the interval slowness at a point **a**, as measured along dipping beds at various depths. These plots correspond to cross-sections along the dashed lines in Figure 3.19. Note that both the amplitudes and the skew change with depth of the reflector.